

May 20, 2008

**HE 1327–2326, an unevolved star with $[\text{Fe}/\text{H}] < -5.0$.
 II. New 3D–1D corrected abundances from a VLT/UVES
 spectrum¹**

Anna Frebel², Remo Collet³, Kjell Eriksson⁴, Norbert Christlieb⁴ and Wako Aoki^{5,6}

ABSTRACT

We present a new abundance analysis of HE 1327–2326, the currently most iron-poor star, based on observational data obtained with VLT/UVES. We correct the 1D LTE abundances for 3D effects to provide an abundance pattern that supersedes previous works, and should be used to observationally test current models of the chemical yields of the first-generation SNe. Apart from confirming the 1D LTE abundances found in previous studies before accounting for 3D effects, we make use of a novel technique to apply the 3D–1D corrections for CNO which are a function of excitation potential and line strength for the molecular lines that comprise the observable CH, NH, and OH features. We find that the fit to the NH band at 3360 Å is greatly improved due to the application of the 3D–1D corrections. This may indicate that 3D effects are actually observable in this star. We also report the first detection of several weak Ni lines. The cosmologically important element Li is still not detected; the new Li upper limit is extremely low, $A(\text{Li}) < 0.62$, and in stark contrast with results not only from

¹Based on observations collected at the European Southern Observatory, Paranal, Chile (Proposal ID 075.D-0048).

²McDonald Observatory, The University of Texas at Austin, 1 University Station, C1400, Austin, TX 78712-0259; anna@astro.as.utexas.edu

³Max-Planck-Institut für Astrophysik, Karl-Schwarzschild-Str. 1, Postfach 1317, D–85741 Garching b. München, Germany

⁴Department of Astronomy and Space Physics, Uppsala University, Box 515, SE-751-20 Uppsala, Sweden; norbert@astro.uu.se

⁵National Astronomical Observatory of Japan, 2-1-21 Osawa, Mitaka, Tokyo, 181-8588 Japan

⁶Department of Astronomical Science, The Graduate University of Advanced Studies, Mitaka, Tokyo, 181-8588 Japan

WMAP but also from other metal-poor stars. We also discuss how the new corrected abundance pattern of HE 1327–2326 is being reproduced by individual and integrated yields of SNe.

Subject headings: Galaxy: halo — stars: abundances — stars: formation — stars: individual (HE 1327–2326) — stars: Population II — early universe

1. Introduction

The interpretation of the chemical abundance patterns of the most metal-poor Galactic stars provides important clues to our understanding of the early Universe and the chemical evolution of the Milky Way. To advance our knowledge about this early time the observed stellar signatures have to be compared with theoretical models of the first cosmic chemical enrichment events. Currently, several groups (Umeda & Nomoto 2003; Chieffi & Limongi 2002; Meynet & Maeder 2002; Meynet et al. 2006; Heger & Woosley 2008) are working on different models of Population III (Pop III) supernovae (SNe). The elemental yields of these SN calculations are used, among other things, for a comparison with individual old metal-poor stars as well as groups of metal-poor stars with similar chemical patterns. These stars are believed to have formed from material exclusively enriched during these early SN events. It can thus be tested whether just a single SN was responsible for the chemical signature in what could be some of the first low-mass stars that formed in the Universe.

The recent discoveries of two stars with iron abundances of $[\text{Fe}/\text{H}]^1 < -5$ (Christlieb et al. 2002, 2004; Frebel et al. 2005; Aoki et al. 2006) have already proved to be ideal test stars for this scenario because they likely formed very early on in the Universe. Umeda & Nomoto (2003) first explained the abundance pattern of HE 0107–5240 with the yields by one single SN undergoing a mixing and fallback mechanism. Subsequent work by Iwamoto et al. (2005) explained HE 1327–2326’s signature in the same manner. However, constructing such a SN model requires as many observed abundances as possible— it is a challenge for this star, as it is extremely iron-deficient, and any spectral lines are very weak (intrinsically, and because of the effective temperature of 6180 K) and difficult to detect.

In this paper, we thus present new abundance measurements of HE 1327–2326, the currently most iron-poor star known (Frebel et al. 2005; Aoki et al. 2006). In 2005, a new VLT spectrum was obtained. The initial discovery spectrum had been taken with the Subaru

¹Where $[\text{A}/\text{B}] = \log(N_{\text{A}}/N_{\text{B}}) - \log(N_{\text{A}}/N_{\text{B}})_{\odot}$ for the number N of atoms of element A and B and \odot refers to the Sun

telescope. The new data have higher S/N and thus already facilitated the determination of the O abundance of HE 1327–2326 from very weak near-UV OH lines (Frebel et al. 2006). The O abundance provided a crucial ingredient for the interpretation of the overall chemical abundance pattern (e.g., Iwamoto et al. 2005; Meynet et al. 2006).

We now use these new VLT data to i) re-determine the abundances of all elements obtained from the Subaru spectrum, ii) to search for (additional) lines of new and already detected elements in the star, iii) to obtain tighter upper limits of existing estimates, and iv) to correct all abundances arising from our 1D model stellar atmosphere analysis for 3D effects (Collet et al. 2006). For some elements, these effects are quite significant. Our measurements, and in particular the new detection of Ni, will provide observational constraints on the yields of the first generations of SNe. Hence, the enrichment scenario of HE 1327–2326 can be further explored, as well as the origins of other extremely metal-poor stars.

2. Observations

A description of the spectroscopic observations can be found in Frebel et al. (2006). We remind the reader that due to the choice of settings the wavelength coverage of the new data is limited to three regions: 3050–3870 Å, 4780–6805 Å, and 5720–9470 Å. The data were reduced with the REDUCE package (Piskunov & Valenti 2002) and subsequently rebinned. The signal-to-noise (S/N) ratios of different wavelength regions are listed in Table 1.

3. Stellar Parameters and Model Atmospheres

We adopt an effective temperature of $T_{\text{eff}} = 6180$ K, as determined in our previous analyses (Frebel et al. 2005; Aoki et al. 2006). Back then it was not possible, however, to distinguish whether HE 1327–2326 would be a subgiant or a main-sequence star. In the meantime, Korn et al. (2008) carried out a new analysis of the Ca I/II ionization equilibrium, which functions as a surface-gravity indicator. As Ca I line formation is prone to departures from LTE (Mashonkina et al. 2007), detailed calculations have been necessary to determine the magnitude of non-LTE effects. Based on the results of a combined analysis of Ca I/II ionization equilibrium and Balmer lines, Korn et al. (2008) conclude that HE 1327–2326 is more likely a subgiant. Hence, for the present work, we will consider the star to be in this evolutionary stage ($\log g = 3.7$).

For the 1D abundance analysis, we use a customary 1D LTE MARCS model stellar atmosphere (B. Gustafsson et al. 2008, in prep.). The model has been constructed with

$T_{\text{eff}} = 6180 \text{ K}$, $\log g = 3.7$, and $v_{\text{micr}} = 2.0 \text{ km/s}$. The complete abundance pattern of the star as derived by Aoki et al. (2006) has been taken into account in the actual modeling. Incidentally, Aoki et al. (2006) also showed that an analysis based on a Kuruzc model with a solar chemical composition scaled down to $[\text{Fe}/\text{H}] = -5$ returns a very similar abundance pattern for HE 1327–2326 (within 0.1–0.2 dex). The mixing-length theory (MLT) formulation for the MARCS model adopted here comes from Henyey et al. (1965).

Recently, Collet et al. (2006) presented 3D–1D corrections to the elemental abundances of HE 1327–2326 derived from individual atomic as well as molecular lines. Such corrections were computed under the assumption of local thermodynamic equilibrium (LTE) by means of a differential 3D–1D analysis based on a 3D hydrodynamical and a 1D MARCS model atmosphere with the same stellar parameters; the authors then applied the results of their 3D–1D analysis to the abundances derived by Aoki et al. (2006) and Frebel et al. (2006) with a 1D analysis to obtain the 3D–1D corrected chemical composition of HE 1327–2326. In the present work, we carry out a differential 3D–1D LTE abundance analysis for the newly observed atomic lines following the same procedure as in Collet et al. (2006). With the availability of such corrections, in this paper we focus on correcting the abundances of HE 1327–2326 for 3D effects to provide the most accurate as possible stellar abundances.

4. Differential 3D–1D abundance analysis

We use convection simulation of a metal-poor turnoff star ($T_{\text{eff}} \simeq 6200 \text{ K}$, $\log g = 4.04$ [cgs], and solar chemical composition scaled down to $[\text{Fe}/\text{H}] = -3$) previously generated by Asplund & García Pérez (2001) as a time-dependent 3D hydrodynamical model atmosphere to study the formation of the atomic and molecular features observed in HE 1327–2326 under the assumption of LTE. The surface convection simulation was carried out with the 3D, time-dependent, compressible, explicit, Eulerian, radiative-hydrodynamical code by Nordlund (1982); Stein & Nordlund (1998). The physical domain of the simulation is a cubic portion of stellar surface about $21 \times 21 \times 7 \text{ Mm}$ in size, large enough to cover about ten granules horizontally and twelve pressure scales in depth. The domain is discretized on a mesh with $100 \times 100 \times 82$ numerical resolution. In terms of continuum optical depth at $\lambda = 5000 \text{ \AA}$, the simulation extends from $\log \tau_{5000} \lesssim -5$ down to $\log \tau_{5000} \gtrsim 6$. Open boundaries are employed vertically and periodic ones horizontally.

The adopted gravity of $\log g = 4.04$ in the 3D simulation is intermediate between what until recently were considered the two best estimates of HE 1327–2326’s surface gravity, i.e., $\log g = 3.7$ (subgiant solution) or $\log g = 4.5$ (dwarf). In solar-like stars, absolute elemental abundances derived from lines of minority species are essentially insensitive to

the exact value of surface gravity (see also Tab. 9 and 10 in Aoki et al. 2006). On the contrary, abundances inferred from lines of majority species (e.g., Fe II) and molecules are more surface gravity dependent. In practice, such surface gravity sensitivity of the derived abundances also changes depending on whether one considers a 3D or 1D model atmosphere for the spectral line formation calculations. Therefore, rather than directly determining the chemical composition of HE 1327–2326 with the exclusive use of the above 3D model, we instead compute *differential* abundances with respect to the results of a 1D abundance analysis based on a 1D MARCS model atmosphere (Gustafsson et al. 1975; Asplund et al. 1997) with identical stellar parameters, input data, and chemical composition as the convection simulation. Figure 1 shows the temperature structure of the 3D model atmosphere adopted here as a function of optical depth; the temperature stratification of the corresponding 1D MARCS model atmosphere is also plotted for comparison. For relatively small changes in terms of surface gravity, such *differential* 3D–1D should in fact be only very marginally sensitive to $\log g$.

While both the 3D simulation and the 1D MARCS model atmosphere are constructed for a solar chemical composition scaled down to $[\text{Fe}/\text{H}] = -3$, in the line formation calculations we assume the chemical abundance pattern to be the same as for HE 1327–2326 (Aoki et al. 2006) when computing ionization and molecular equilibria and continuous opacities; as a rule, only the abundances of the trace elements are varied when calculating line opacities. In fact, using a scaled solar chemical composition with $[\text{Fe}/\text{H}] = -3$ would lead to overestimate the abundance of elements with low ionization potentials and, in turn, the electron density, therefore affecting ionization balance, continuous opacities, and, ultimately, line strengths. In addition, when computing background opacities and electron density, we adopt C, N, and O abundances midway between the values derived by Aoki et al. (2006) and Frebel et al. (2006) for the subgiant and dwarf solutions: this is done in order to compensate for the particular choice of surface gravity in the 3D simulation and corresponding 1D model.

We compute flux profiles for all the spectral lines from neutral and singly-ionized metals presently observed in HE 1327–2326. We also consider a set of “fictitious” CH, NH, and OH (see e.g., Collet et al. 2006, 2007) lines with varying lower excitation potentials (0 to 3.5 eV) and $\log gf$ values within the range typical for the observed molecular bands in this study. From the full 3D simulation we select a 60 minutes long (stellar time) sequence of 30 snapshots equidistant in time. We decrease the horizontal resolution of the simulation from 100×100 to 50×50 to reduce the computational load and time of the 3D line formation calculations; we also interpolate all simulation snapshots to a finer depth-scale in order to increase the resolution of the atmospheric layers ($\log \tau_{5000} \lesssim 2.5$) to improve the numerical accuracy of the radiative transfer solution. For each line we solve the radiative transfer equation for all grid-points across the horizontal plane and along 33 directions (4 μ -angles,

8 ϕ -angles, and the vertical), after which we perform a disk-integration and a time-average over all selected 3D snapshots. We use 70 wavelength points to resolve each line profile. The source function for lines and continuum is approximated with the Planck function at the local temperature and scattering is treated as true absorption. Continuous opacities come from the Uppsala package (Gustafsson et al. 1975, and subsequent updates), the equation-of-state from Mihalas et al. (1988, and subsequent updates), the partition data for atoms and ions from Irwin (1981) and for molecules from Sauval & Tatum (1984). The same radiative transfer solver and input data are also used for spectral line formation calculations with the 1D model atmosphere. In addition, for the 1D case, we adopt a micro-turbulence of $\xi = 1.6 \text{ km s}^{-1}$ for the turnoff star. We stress that no micro- nor macro-turbulence parameters enter the 3D spectral line synthesis calculations: only the velocity fields predicted by the actual 3D simulation are used to reproduce non-thermal line broadening and asymmetries associated with convective Doppler shifts.

For each line, we quantify the impact of the 3D model in the analysis, by varying the abundance of the trace element independently in the 1D and 3D line formation calculations until the measured equivalent width is matched: the difference between the 3D and 1D derived abundances then defines the 3D–1D abundance correction for the given line.

Before proceeding, we caution that the actual 3D–1D abundance corrections depend in part on the choice of 1D model atmosphere in the differential abundance analysis. Ideally, one should compute the differential corrections using a 1D model atmosphere that relies on exactly the same input physics and treatment of radiative transfer as the convection simulation. Although the input physics of the MARCS model atmosphere adopted here does not depart substantially from the one used in the 3D case, some differences in practice still exist. In particular, contrary to the 3D hydrodynamical simulation, scattering is treated correctly as such and not as true absorption in the 1D MARCS model. Also, the two kinds of models rely on slightly different equations-of-state. Finally, while the sources of continuous and line opacities are namely the same (Gustafsson et al. 1975; Kurucz 1992, 1993), during the 3D simulation opacities are grouped in four opacity bins to ease the computational burden of the radiative transfer calculations. To estimate what the effect of the particular choice of model atmosphere is on the 3D–1D corrections, we also performed a 3D–1D differential abundance analysis based on a 1D ATLAS model atmosphere (Kurucz 1993) with same stellar parameters and chemical composition as the 3D model. Because of the slightly higher temperature of the 1D ATLAS model atmosphere in line formation regions, the resulting 3D–1D abundance corrections for all elements are systematically shifted 0.05 to 0.1 dex downwards (i.e., toward more negative values) with respect to the differential analysis based on the 1D MARCS model. We finally note that there is no dependence of the 3D–1D corrections on the adopted micro-turbulence of the 1D model (see Aoki et al. 2006), nor any significant

dependency on MLT. Molecular lines, for which the 3D–1D corrections are the largest, form in the upper layers of the photosphere where the type of mixing-length prescription is not expected to have an effect on the atmospheric structure.

5. Chemical Abundances

We now describe the abundances of individual elements as far as the new analysis is concerned. Details on the 3D–1D corrections and our new technique to apply those to abundances derived from molecular features are given where appropriate. The new abundance pattern is summarized in Table 2, and in Figure 2 our results for HE 1327–2326 are compared with those for HE 0107–5240, the other star with $[\text{Fe}/\text{H}] < -5$. We also refer the reader to Aoki et al. (2006); they presented a detailed discussion of the HE 1327–2326’s chemical pattern as well as a comparison with other metal-poor stars. A detailed uncertainty analysis for the abundances of the star was also presented (their Table 10) and will not be repeated here.

5.1. Line Data and Analysis Techniques

Atomic line data for the abundance analysis have been taken from Aoki et al. (2006) and references therein, substituted with lines from Christlieb et al. (2004) and references therein, and from the Vienna Atomic Line Database (VALD; Kupka et al. 1999). Molecular line data have been taken from B. Plez (priv. communication) for CH and Gillis et al. (2001) for OH. For NH we are using the linelist of Kurucz (1993), but add a 0.4 dex to the gf-values to fit the solar spectrum (see Aoki et al. 2006 for details). For CH and OH we use dissociation energies of 3.47 eV and 4.39 eV, respectively (Huber & Herzberg 1979). For NH we employ 3.37 eV (Bauschlicher & Langhoff 1987).

Equivalent widths are measured from the spectrum by fitting Gaussian profiles to the generally very weak lines. Upper limits (3σ) for equivalent widths are derived from $\sigma = wn_{pix}^{1/2}/(S/N)$ (where w is the pixel width, n_{pix} is the number of pixels across the line (e.g., where a weak line would reach the continuum if a line was present), and S/N is per pixel; Bohlin et al. 1983). The measurements and upper limits for HE 1327–2326 are presented in Table 3. Apart from hydrogen and molecular lines of CH, NH, and OH we now find 44 atomic lines in the spectrum of eight elements (Na, Mg, Al, Ca, Ti, Fe, Ni, Sr) and are able to determine upper limits of nine additional elements. The previous analysis by Aoki et al. (2006) identified 22 atomic lines.

5.2. Iron

In the Subaru spectrum seven weak FeI lines were detected (Aoki et al. 2006). The strongest line was measured to have an equivalent width of 6.8 m\AA . As already reported in Frebel et al. (2006) the new data confirm the presence of six of the seven lines (the wavelength of one line is not covered by our VLT spectrum). Additionally, we detect four new lines and report tentative detections of another three. This brings the total of detected lines to 11 FeI lines from which the metallicity is deduced. We note that the average that includes the abundances of the tentative FeI lines agrees within 0.03 dex with the average from the 11 detected lines only. Figure 3 shows the detected and tentatively detected 13 FeI lines in the VLT spectrum.

Based on the new equivalent width measurements together with the one from Aoki et al. (2006) for the line that is not covered, we find HE 1327–2326 to have a 1D LTE Fe abundance² of $[\text{Fe}/\text{H}] = -5.66$, the same as the previous result reported in Aoki et al. (2006).

In this work we are now applying 3D–1D LTE corrections to our 1D LTE abundances. Within the LTE framework, the average 3D–1D Fe abundance correction for FeI lines is negative (-0.24 ; Collet et al. 2006). Thus, the FeI abundance of HE 1327–2326 is reduced to $[\text{Fe}/\text{H}] = -5.90$. To illustrate why the 3D–1D Fe abundance correction from FeI lines is negative, in Figure 4 we compare the fraction of neutral to total iron in the 3D and 1D model atmospheres. While in the 1D model iron is essentially all ionized to FeII, in 3D a significant fraction of iron is in neutral form in the upper photospheric layers because of the cooler surface temperature stratification predicted by the 3D metal-poor convection simulation (see e.g., Asplund & García Pérez 2001). Hence, at a given Fe abundance and under the assumption of LTE, FeI lines appear stronger in the 3D line formation calculations than they do in 1D. This also implies that the same equivalent width of a FeI line is matched by a lower Fe abundance in 3D than in 1D. Alternatively, one can also show that the same FeI line forms at different depths in the 3D and 1D models. Figure 5 shows the contribution function $\mathcal{C}_I(\tau_\lambda) = \mathcal{S}_\lambda(\tau_\lambda) \exp(-\tau_\lambda)$ to the outgoing intensity at line center in the vertical direction for the FeI line at $\lambda = 3859.9 \text{ \AA}$ in the two models. It is apparent from the figure that, in 3D, the main contribution to the outgoing vertical intensity for the FeI line is given by layers lying higher up in the atmosphere where the temperature differences between 3D and 1D structures are larger.

²This value has essentially already been published in Frebel et al. (2006). We simply give more details on the derivation of this value, and also report the detection of additional FeI lines.

We note that any possible non-LTE effects present within the 3D FeI line formation calculations are currently unexplored, but likely to be positive (Asplund 2005). For completeness, we remind the reader that in previous works the measured FeI abundance was corrected by +0.2 dex to account for 1D non-LTE effects in FeI (Collet et al. 2006 predict for FeI a much stronger departure from LTE). In principle, FeII lines should be the preferred Fe abundance indicator as they are usually expected to be less sensitive to departures from LTE. However, even the strongest FeII lines are expected to be extremely weak in HE 1327–2326 given its stellar parameters and composition. In fact, no FeII line could be detected in either the Subaru or in the new VLT spectrum. The 3D–1D corrected upper limit is $[\text{FeII}/\text{H}] < -5.40$. We can also place an upper limit on the FeI 3D non-LTE effect of $\lesssim 0.5$. This is derived under the assumption that there is an ionization equilibrium of FeI and FeII if the surface gravity of $\log g = 3.7$, as derived from an isochrone, is correct, and that FeII lines are not affected by non-LTE. In the absence of FeII lines, Ca is the only element detectable in two ionization stages. As mentioned above, this offers the possibility of using CaI/II as a surface-gravity indicator (Korn et al. 2008).

5.3. CNO elements

Carbon, nitrogen and oxygen abundances for HE 1327–2326 were derived by Aoki et al. (2006) (C and N; from the Subaru spectrum) and then by Frebel et al. (2006) (C and O; from the VLT spectrum). For the latter 1D LTE analysis, corrections were suggested for all three elements to account for 3D model atmosphere effects. The estimated 3D–1D corrections were mostly based on works described in Asplund (2005) and references therein.

Molecular features consist of many different lines with a variety of excitation potentials. As 3D–1D abundance corrections depend in general on the excitation potentials of the contributing lines, the final 3D–1D correction to the 1D abundance of the trace elements in the molecular features has to be an appropriate average of the 3D–1D abundance corrections derived for individual lines. Collet et al. (2006) computed 3D–1D corrections for a few fictitious lines of CH, NH, and OH with selected excitation potentials. By using fictitious lines, the 3D–1D corrections to the CNO abundances could be studied without resorting to a full spectrum synthesis with a 3D model atmosphere. Here we extend the study by Collet et al. (2006) to consider a more comprehensive range of lower excitation potentials and $\log gf$ values of the CH, NH, and OH lines. Figures 6 and 7 show the 3D–1D LTE corrections to the CNO abundances derived from the molecular lines as a function of line strength and excitation potential. In the case of CH and OH lines, 3D–1D LTE C and O abundances are also plotted as a function of the corrections to oxygen and carbon abundances, respectively.

The magnitudes of abundance corrections derived from molecular lines depend in fact not only on the different photospheric structures of the 3D and 1D model atmospheres but also on the overall chemical composition and details of the molecular equilibrium. In particular, the line strengths of CH and OH lines are sensitive to both the carbon *and* oxygen abundances assumed in the spectral line formation calculations because of the competing formation of CO molecules. Temperatures in the upper photospheric layers of the metal-poor 3D model atmosphere adopted here are on average considerably lower than in the corresponding 1D model. At low temperatures ($\lesssim 3700$ K), significant fractions of C and O become locked in CO molecules. Thus, for instance, if one were to increase slightly the *oxygen* abundance in the line formation calculations with the metal-poor 3D model, that would then lead to the formation of more CO and therefore reduce the amount of *carbon* available for other molecules such as CH. Hence, at a fixed carbon abundance, but with higher oxygen abundance, CH lines would become *weaker*, and the associated 3D–1D LTE C abundance corrections would in turn be *larger* (i.e., more negative). The same argument holds for the variation of the equivalent widths of OH lines as a function carbon abundance.

In order to apply the 3D–1D corrections to the CNO abundances in a more suitable way, we developed a new technique. We first interpolate in between the 3D–1D abundance corrections given as a function of excitation potential and line-strength to obtain appropriate corrections for all individual lines that comprise the molecular feature of interest. The abundance corrections so computed (in *dex*) are then *subtracted* (the negative corrections) from the $\log gf$ values for all lines in our linelist. The observed spectrum is then re-synthesized with the new “3D-adjusted” linelist. We call this procedure “3D-aided spectrum synthesis”.

Before we proceed further, however, a number of tests have to be made: i) We re-determine the “1D” abundances from the new VLT spectrum for a comparison with previously published values. ii) We synthesize the spectrum with the new 3D-adjusted linelist. iii) We compare the synthetic fit derived from the original “1D” linelist with the one computed with the new 3D-adjusted linelist to explore the influence of the different 3D–1D corrections on different excitation potentials. The results are shown in Figures 8, 9, and 10.

We also caution the reader that the here computed average 3D–1D abundance corrections are only valid for the considered wavelength range (because of, e.g., the specific combination of lower excitation potentials of the contributing lines, the continuous opacities at these wavelengths, etc.), and may thus not apply in general to other molecular features in different regions of the spectrum. Finally, we also remind that any possible 3D non-LTE or non-equilibrium chemistry effects remain unexplored at this point in time, but are expected to be positive (Asplund 2005) and therefore reduce (i.e., make less negative) the effective 3D–1D correction to CNO abundances.

5.3.1. Carbon

The 1D C abundance was already determined from the VLT spectrum by Frebel et al. (2006). In the meantime, however, a new CH linelist has become available (B. Plez, priv communication, but see Frebel et al. 2007a for some technical details) which yields much improved syntheses for metal-poor stars. Hence, we use the new linelist, and derive the C abundance from the G-band head at $\sim 4313 \text{ \AA}$. The newly derived 1D abundance³ of $\log \epsilon = 6.90$ agrees very well with previous values of $\log \epsilon = 6.90$ (Frebel et al. 2005), $\log \epsilon = 6.99$ (Aoki et al. 2006) and $\log \epsilon = 6.86$ (from various CH features; Frebel et al. 2006).

The excitation potentials of the participating lines in the G-band spectral region are of a similar level (top panel in the figure), that results in a almost constant 3D–1D correction across that region. Hence, the variation in abundance between the 1D and 3D-aided synthetic spectra does not exceed ~ 0.05 dex (see the second panel from the top in Figure 8). The fit with the 3D-adjusted linelist to the individual lines of the G-band is, however, slightly improved due to the changes in line strengths (compare with second panel from the bottom in the figure). The overall fit to the data is excellent, and makes it easy to accurately determine a mean 3D–1D correction of C of -0.69 (bottom panel of figure). The final C abundance is $[\text{C}/\text{Fe}] = 3.78$ dex. Finally, concerning the $^{12}\text{C}/^{13}\text{C}$ ratio, unfortunately the VLT data do not cover appropriate wavelengths to re-measure this important ratio.

5.3.2. Nitrogen

The 1D N abundance was determined from the NH band at 3360 \AA for a comparison with the value obtained from the Subaru discovery spectrum. Our new fit is much improved due to increased S/N in this spectral region (now ~ 200 red-ward of the band). The newly derived 1D abundance of $\log \epsilon(N) = 6.79$ agrees with the values of 6.68 and 6.83 presented in Frebel et al. (2005)⁴ and Aoki et al. (2006).

Figure 9 shows the excitation potentials of the molecular lines that comprise the NH fit. There is a gradual change to higher excitation potentials from 3357 to 3365 \AA . From the comparison of the 1D and 3D-aided synthetic spectra it can be seen that the change in excitation potentials results in the 3D-aided synthetic spectrum having slightly stronger lines blue-ward ($\sim +0.1$ dex) of the main NH feature at 3360 \AA and slightly weaker (~ -0.2 dex)

³Where $\log \epsilon(X) = \log(N_X/N_H) + 12.0$

⁴For NH, a dissociation energy of 3.47 was used. If a value of 3.37 is employed the abundances becomes $\log \epsilon(N) = 6.78$.

lines on the red side (see second panel from top in Figure 9). Irrespective of any resulting abundance, this effect causes an improvement of the new fit to the observed NH spectral region compared with the original 1D linelist fit.

This effect can not be “fixed” with a simple abundance offset since it would be the same for all participating lines irrespective of excitation potential. We note that this apparent improvement can not be accounted to continuum normalization issues since the continuum points of the synthetic spectra match the observed spectrum very well. If the continuum of the observed spectrum were determined incorrectly, those points should not be reproduced by the fit. We checked the Subaru spectrum, and as can be seen in Figure 7 of Aoki et al. (2006), the effect of the fit significantly underproducing the observed spectrum on the blue side, and very slightly overproducing it on the red side (their best fit is aimed at reproducing the red side) is present there as well. From this comparison we conclude that it is not a data reduction effect. We also tested if that effect would result from the dependence of the 3D–1D correction on line strength, but found it to be negligible. We then investigated the influence of the effective temperature on relative line strengths, which in turn depend on their excitation potentials. We changed the effective temperature of the model atmosphere by -400 K, and fitted the blue side of the NH band again. On the red side the new fit did almost match the fit with the original model atmosphere. The difference on the red side was only about one third of the difference between the 1D and 3D-aided fits. It follows that the apparent improvement of the fit to the data is still present, and can not be explained with a temperature effect only.

It may thus be possible that the 3D effect can be directly seen in the NH band, due to a fortuitous distribution of excitation potentials. The overall 3D–1D correction over the NH range is -0.69 dex. A larger, or smaller, correction would, again, result in a less optimal reproduction of the observed data, thus suggesting that such a large 3D correction is correct and necessary to obtain a more accurate N abundance for the star. The final N abundance is $[N/Fe] = 4.28$.

We note though, that we cannot exclude possible systematic effects in the present 3D–1D differential analysis due to neglected departures from LTE and from chemical equilibrium at the local temperature. Hypothetically, if such departures affected all 3D–1D corrections for individual molecular lines (with different excitation potentials) by an approximately constant factor, then a re-scaling of all gf-values in the 3D-adjusted linelist by the inverse of the same factor would still lead to a very good fit of the molecular band but with a different final 3D correction. The success in the present 3D analysis thus lies in the fact that the relative line-to-line scatter in the abundances derived from individual lines in the molecular feature is very much reduced compared with the 1D analysis.

Often, synthetic fits to observed molecular bands are not fully satisfactory. This is always accounted for in terms of uncertainties in the molecular line data used to generate the synthetic spectra. While this may still be true in the case of NH, the uncertainties would be the same for both the original 1D and the 3D-adjusted linelists, and only affects our conclusions in the sense that the molecular NH data, i) either is better than previously thought, or ii) a different, yet unexplored, effect is responsible for the better fit to the observed data. The application of 3D–1D corrections in the same way as presented here should be further investigated for other metal-poor stars to test whether this is a more general effect or limited to the extreme case of HE 1327–2326. We note that while the 3D–1D corrections for CNO elements HE 0107–5240 are similarly large, the S/N ratio of the data at $\sim 3360 \text{ \AA}$ is not yet sufficient to infer a similar effect for this object (N. Christlieb et al. 2008, in prep.).

5.3.3. Oxygen

The O abundance determination from the VLT data was already described in detail by Frebel et al. (2006). Apart from the offset in abundance caused by the application of the 3D–1D correction, there generally is good agreement between the two fits (see the second panel from the top in Figure 10). The overall 3D–1D correction for OH as determined in this work is -0.72 dex, and thus a slightly lower than what was estimated (-0.9 dex) in Frebel et al. (2006). The final O abundance is $[O/Fe] = 3.42$.

5.4. Lithium and Beryllium

The LiI doublet at 6707 \AA is *still* not detected in this relatively unevolved star. From the extremely high S/N (~ 600 per pixel) data we are able to derive a new 3σ upper limit of $\log \epsilon(\text{Li}) = A(\text{Li}) < 0.70$ from our 1D analysis; this is further reduced to $A(\text{Li}) < 0.62$ by application of the 3D correction. Figure 11 shows the Li spectral regions overplotted with synthetic spectra of different abundances. This is significantly lower (i.e., by 1 dex) than the previous limit of $\log \epsilon(\text{Li}) = 1.6$ (Aoki et al. 2006). Other unevolved metal-poor stars with $[Fe/H] \sim -3.5$ have Li values around $\log \epsilon(\text{Li}) \sim 2.0$ (e.g., Ryan et al. 1999). These objects have been used to infer the primordial Li abundance, which can be compared to the value expected from the baryon-to-photon ratio inferred from WMAP data (Spergel et al. 2007), $\log \epsilon = 2.6$. The discrepancy between the WMAP result and the observed Li abundance in metal-poor stars has amply been established, so we shall not further elaborate on it here. We only note that even though the Li I lines, in general, are prone to non-LTE effects, they are likely to be far too small (~ 0.1 dex) to bridge the gap between the Li abundance of

HE 1327–2326 and that of other metal-poor star as well as the WMAP-inferred value. Also, gravitational settling of lithium as a possible solution to the discrepancy is not sufficient (Korn et al. 2008) It is thus very surprising that the upper limit of HE 1327–2326 is not only lower than the WMAP result but also considerably lower (by more than 1 dex) than values derived from other metal-poor star with similar evolutionary status. This means that either all of this star’s Li was destroyed during its lifetime on the main-sequence, or the star was born from a Li-depleted material.

Piau et al. (2006) developed a picture where a large fraction of the early interstellar medium (ISM) is “recycled” through massive rotating Pop III stars with the consequence that Li depleted material is deposited back into the ISM through stellar winds. The first low-mass stars would primarily form in the wake of those Li-deficient, but CNO rich winds (Meynet et al. 2006, but also see above). The new lower limit of Li (together with high CNO) in HE 1327–2326 is in line with this theory. If this scenario were correct, any (future) observations of yet-to-be-found dwarfs with metallicities of $[\text{Fe}/\text{H}] \lesssim -4.0$ should indeed reveal strong Li-depletion. Other options for the Li deficiency have been explored in Aoki et al. (2006), and include rapid rotation and HE 1327–2326 being a member of a binary system. As for the binary system, continued radial velocity monitoring does not (yet) suggest the presence of any companion.

Beryllium is another light, fragile element observed in very metal-poor turn-off stars. Standard Big-Bang nucleosynthesis models do not predict a significant yield of this element. Be is destroyed at $T = 3.5 \times 10^6$ K, and is thus slightly more robust than Li. Hence, if the Be abundance, or a strong upper limit of the abundance, is determined for HE 1327–2326, that could provide important clues as to why the Li abundance in the star is so extremely low.

In Figure 12 we show the spectral region of the two strongest Be II lines in the near UV. As can be seen there is a (noise) peak at the right wavelength of the 3131 Å line. However, the S/N in this spectral region is low, so that we cautiously adopt an upper limit of $A(\text{Be}) < -1.2$. This value is as low as the Be abundances measured for extremely metal-poor stars (e.g., Boesgaard & Novicki 2006). Thus, we can not derive any definitive conclusion from the upper limit of the Be abundance for the depletion of Li in this object.

5.5. Other elements

For the lines that were previously measured by Aoki et al. (2006), there generally is good agreement between their and our equivalent widths (there is no significant offset). Figure 13

shows a comparison of the two measurements for the lines in common. We detected many more lines in the spectrum which confirm the abundances as derived from the Aoki et al. lines. We can also report the first detection of four Ni lines in HE 1327–2326 (see Figure 14). Previously only an upper limit could be derived, but now four weak lines are detected. The equivalent width measurements and upper limits are presented in Table 3, while the resulting abundances are given in Table 2.

We also re-determined upper limits for Cr, Co, and Zn. The limits are much tighter (by ~ 0.4 to 0.8 dex) than obtained from the Subaru spectrum, due to the increased S/N ratio of the VLT data particularly in the blue spectral region. New upper limits for Be, Sc and V could also be derived. Our new upper limits, together with the detection of Ni, are of interest when comparing the overall abundance pattern with theoretical calculations of SN yields. We will return to this point in § 6.

Unfortunately, our spectrum does not cover suitable lines of Mn, Si, S, Sr, Ba and Eu. That leaves us with no information about Si and S, and only the previous values from the Subaru spectrum in the case of Mn, Sr and Ba. For Mn, the second strongest line yields the same upper limit as has been previously derived from the strongest line at 4020 \AA . The same is the case for Ba. A weaker line at 4943 \AA line is covered by the red setting. Figure 15 shows the Ba spectral regions overplotted with synthetic spectra of different Ba abundances. The inferred upper limit yielded almost the same as was reported in Aoki et al. (2006) based on the resonance line at 4554 \AA . The resulting ratio is $[\text{Sr}/\text{Ba}]_{3\text{D}} > -0.29$.

This limit is already higher than what is found in typical r-process enhanced metal-poor stars (-0.4 to -0.5 ; Sneden et al. 1998; Hill et al. 2002; Frebel et al. 2007a). The value is certainly inconsistent with ratios found in s-process-rich stars, which have much lower $[\text{Sr}/\text{Ba}]$ values. Large excesses of light neutron-capture elements are also found in extremely metal-poor stars, whose abundance ratios of light to heavy neutron-capture elements, such as Sr/Ba, are significantly higher than the ratios of the known r-process yields (e.g., Aoki et al. 2005). The detailed abundance patterns of such stars have been recently determined by Honda et al. (2006, 2007). If the Sr of HE 1327–2326 were related to the process that provided extremely metal-poor stars with light neutron-capture elements, the Sr overabundance could be a key to understanding the nucleosynthesis mechanism of the progenitor object (e.g., Fröhlich et al. 2006). Such process is associated with explosive nucleosynthesis, and is thus compatible with the pre-enrichment scenario by a previous generation SN as explanation for the overall abundance pattern rather than through mass transfer across a binary system (see below). As for Eu, since the strongest line at 4129 \AA is not covered, only a meaningless upper limit of $[\text{Eu}/\text{Fe}] < 4.1$ could be derived from a line at 6645 \AA .

For completeness, we also provide the upper limits derived from the OI triplet and

forbidden OI lines, as presented in Frebel et al. (2006). Upper limits on the equivalent width and abundances are listed in Tables 3 and 2.

6. Discussion and Conclusions

We have presented an abundance analysis of the currently most Fe-poor star, HE 1327–2326, based on the currently best available observational data obtained with VLT/UVES. In an attempt to obtain the best possible abundances from those data, we have combined our 1D abundances with state-of-the-art 3D–1D model atmosphere corrections. Hence, these abundances supersede our previous measurements. We recommend using these new 3D–1D corrected LTE abundances for future modeling of the abundance pattern of HE 1327–2326.

Figure 16 summarizes all abundances measurements for the star published to date. We plot the “best available” values at the time, i.e., 1D abundances with non-LTE corrections where available in the older cases, and LTE abundances with differently determined 3D corrections in the newer studies. The Fe abundance differs in these works, so that we compare $[X/H]$ values which leave Fe as “free parameter”. The 3D–1D corrected abundances are somewhat shifted towards lower values compared with the 1D abundances. The biggest differences are found among the CNO elements ($\Delta \sim -0.7$) whereas for other elements the differences between 1D and 3D analyses are less pronounced. We note that when comparing $[X/Fe]$ measurements, because of the different $[Fe/H]$ values, some of those differences in $[X/H]$ are canceled out. This fact should be kept in mind when comparing the overall abundance pattern with theoretically derived abundances predictions based on SN yields.

Several groups of authors have already employed the (in the most cases the old) abundances to test current scenarios for the chemical yields of the first-generation SNe. In order to compare how well all these predictions reproduce our new 3D–1D corrected abundances presented here, we plot them all in Figure 17. We note that all the above interpretations assume that the star is not a member of a binary system. This is indeed supported by ongoing radial velocity measurements of HE 1327–2326. Two measurements, one from 2007 (D. Lai, priv. comm.) and one from 2008 agree with the previous data (Frebel et al. 2006) and does not indicate any significant change of the radial velocity.

Iwamoto et al. (2005) were the first authors to compare the 1D abundances of HE 1327–2326 (Frebel et al. 2005) with their yields of a $25 M_{\odot}$ Pop III hypernova, for given mixing and fallback parameters. Particularly, the high CN abundance together with the elevated Mg abundance were well reproduced by their yields. An updated fit was presented in Tominaga et al. (2007) after the O abundance (with estimates for the 3D–1D correction) of HE 1327–2326

had been determined (Frebel et al. 2006). Hence, this model now particularly well fits our new CNO abundances. Na, Mg, Al, Ca and Fe abundances are well reproduced, too. The new abundance of Ni (3D–1D corrected) also agrees with their predicted Ni yield.

Meynet et al. (2006) investigated mass loss by a massive ($60 M_{\odot}$) rotating Pop III star, and the chemical yields of the subsequent SN explosion. They find that from the combined yields of the stellar wind and the SN, the highly elevated 1D CNO pattern of HE 1327–2326 (Frebel et al. 2005) and that of other metal-poor stars can qualitatively be reproduced. In their “wind-only” model, a high N abundance can be achieved, although all other elements considered (except Al) are produced in insufficient quantities to reproduce the observed abundance pattern.

Heger & Woosley (2008) have computed new chemical yields for a range ($10\text{--}100 M_{\odot}$) of Pop III SNe. They are fitting the observed abundances of HE 1327–2326 (Aoki et al. 2006) with either the yield of a single SN or the integrated yields of a range of SNe for a given initial mass function. For various progenitor masses (mass ranges), explosion energies, and mixing parameters the abundance pattern can be roughly reproduced. The best fit model for a single SN requires a $21.5 M_{\odot}$ progenitor, while the best fit model for integrated yields stems from the range $15\text{--}35 M_{\odot}$ of progenitors. Overall, this is a similar progenitor mass as Iwamoto et al. (2005) suggested. In Figure 17 we show the “best single stars” fit (Panel A in their Figure 14; Heger & Woosley 2008) in comparison with our new abundances. Overall, the fit is in reasonable agreement with the data and provides an interesting counterpart to the work of Tominaga et al. (2007).

Recently, Frebel et al. (2007b) used C and O abundances of metal-poor stars for a comparison with theoretical predictions for the critical metallicity that is required to facilitate low-mass star formation in the early Universe. Based on the theory of fine-structure line cooling, it was predicted that all stars with $[\text{Fe}/\text{H}] \lesssim -4.0$ should have elevated C and/or O abundances and have $D_{\text{trans}} = \log(10^{[\text{C}/\text{H}]} + 10^{[\text{O}/\text{H}]}) > -3.5$ dex. The new 3D–1D corrected abundances of HE 1327–2326 presented here lead to $D_{\text{trans}} = -2.18$ dex, well above the critical value.

7. Outlook

To improve our understanding of the conditions of the early Universe, and to put all the above theories to further critical observational tests, clearly, more stars are needed with metallicities of $[\text{Fe}/\text{H}] \lesssim -4$. Norris et al. (2007) recently reported the discovery of a giant with $[\text{Fe}/\text{H}] = -4.75$. In particular, more giants should be sought at the lowest metal-

licities because their (lower) temperature, at a given abundance, allows for stronger lines that can be detected more easily. The Fe lines in the subgiant HE 1327–2326 are only barely detectable because of its hotter temperature. Further ultra-metal-poor stars to be discovered in the future will likely be fainter than HE 1327–2326 ($B \sim 14.0$ mag) and even HE 0107–5240 ($B \sim 15.6$ mag), which imposes yet another challenge when it comes to obtaining the necessary high S/N spectra to measure very weak spectral lines particularly in the blue spectral region. Detailed studies of larger samples of stars at $[\text{Fe}/\text{H}] < -5.0$ will therefore require 30 m class telescopes, which will make possible such difficult but extremely important observations.

We thank Martin Asplund for discussions on abundance analyses based on 3D model stellar atmospheres and an anonymous referee for valuable suggestions regarding our new 3D–1D abundance correction technique. A. F. thanks Uppsala Astronomical Observatory for its hospitality during parts of the write-up of this paper. She acknowledges support through the W. J. McDonald Fellowship of the McDonald Observatory. N. C. acknowledges financial support by Deutsche Forschungsgemeinschaft through grants Ch 214/3 and Re 353/44. He is a Research Fellow of the Royal Swedish Academy of Sciences supported by a grant from the Knut and Alice Wallenberg Foundation.

Facilities: VLT:Kueyen (UVES)

REFERENCES

- Aoki, W., Frebel, A., Christlieb, N., Norris, J. E., Beers, T. C., Minezaki, T., Barklem, P. S., Honda, S., Takada-Hidai, M., Asplund, M., Ryan, S. G., Tsangarides, S., Eriksson, K., Steinhauer, A., Deliyannis, C. P., Nomoto, K., Fujimoto, M. Y., Ando, H., Yoshii, Y., & Kajino, T. 2006, *ApJ*, 639, 897
- Aoki, W., Honda, S., Beers, T. C., Kajino, T., Ando, H., Norris, J. E., Ryan, S. G., Izumiura, H., Sadakane, K., & Takada-Hidai, M. 2005, *ApJ*, 632, 611
- Asplund, M., Gustafsson, B., Kiselman, D., & Eriksson, K. 1997, *A&A*, 318, 521
- Asplund, M., & García Pérez, A. E. 2001, *A&A*, 372, 601
- Asplund, M. 2005, *ARA&A*, 43, 481
- Asplund, M., Grevesse, N., & Sauval, A. J. 2005, in *ASP Conf. Ser. 336: Cosmic Abundances as Records of Stellar Evolution and Nucleosynthesis*, 25

- Bauschlicher, Jr., C. W. & Langhoff, S. R. 1987, *Chem. Phys. Lett.*, 135, 67
- Boesgaard, A. M. & Novicki, M. C. 2006, *ApJ*, 641, 1122
- Bohlin, R. C., Jenkins, E. B., Spitzer, L., York, D. G., Hill, J. K., Savage, B. D., & Snow, T. P. 1983, *ApJS*, 51, 277
- Chieffi, A. & Limongi, M. 2002, *ApJ*, 577, 281
- Christlieb, N., Bessell, M. S., Beers, T. C., Gustafsson, B., Korn, A., Barklem, P. S., Karlsson, T., Mizuno-Wiedner, M., & Rossi, S. 2002, *Nature*, 419, 904
- Christlieb, N., Gustafsson, B., Korn, A. J., Barklem, P. S., Beers, T. C., Bessell, M. S., Karlsson, T., & Mizuno-Wiedner, M. 2004, *ApJ*, 603, 708
- Collet, R., Asplund, M., & Trampedach, R. 2006, *ApJ*, 644, L121
- Collet, R., Asplund, M., & Trampedach, R. 2007, *A&A*, 469, 687
- Frebel, A., Aoki, W., Christlieb, N., Ando, H., Asplund, M., Barklem, P. S., Beers, T. C., Eriksson, K., Fechner, C., Fujimoto, M. Y., Honda, S., Kajino, T., Minezaki, T., Nomoto, K., Norris, J. E., Ryan, S. G., Takada-Hidai, M., Tsangarides, S., & Yoshii, Y. 2005, *Nature*, 434, 871
- Frebel, A., Christlieb, N., Norris, J. E., Aoki, W., & Asplund, M. 2006, *ApJ*, 638, L17
- Frebel, A., Christlieb, N., Norris, J. E., Thom, C., Beers, T. C., & Rhee, J. 2007a, *ApJ*, 660, L117
- Frebel, A., Johnson, J. L., & Bromm, V. 2007b, *MNRAS*, 380, L40
- Fröhlich, C., Martínez-Pinedo, G., Liebendörfer, M., Thielemann, F.-K., Bravo, E., Hix, W. R., Langanke, K., & Zinner, N. T. 2006, *Physical Review Letters*, 96, 142502
- Gillis, J. R., Goldman, A., Stark, G., & Rinsland, C. P. 2001, *Journal of Quantitative Spectroscopy & Rad. Transfer*, 68, 225
- Gustafsson, B., Bell, R. A., Eriksson, K., & Nordlund, Å. 1975, *A&A*, 42, 407
- Heger, A. & Woosley, S. E. 2008, *ApJ*, submitted, astro-ph/0803.3161,
- Henyey, L., Vardya, M. S., & Bodenheimer, P. 1965, *ApJ*, 142, 841
- Hill, V., Plez, B., Cayrel, R., Nordström, T. B. B., Andersen, J., Spite, M., Spite, F., Barbuy, B., Bonifacio, P., Depagne, E., François, P., & Primas, F. 2002, *A&A*, 387, 560

- Honda, S., Aoki, W., Ishimaru, Y., & Wanajo, S. 2007, *ApJ*, 666, 1189
- Honda, S., Aoki, W., Ishimaru, Y., Wanajo, S., & Ryan, S. G. 2006, *ApJ*, 643, 1180
- Huber, K. P. & Herzberg, G. 1979, *Molecular Spectra and Molecular Structure, Vol. IV, Constants of Diatomic Molecules* (New York: Van Nostrand Reinhold)
- Irwin, A. W. 1981, *ApJS*, 45, 621
- Iwamoto, N., Umeda, H., Tominaga, N., Nomoto, K., & Maeda, K. 2005, *Science*, 309, 451
- Korn, A. J., Mashonkina, L., Richard, O., Frebel, A., Aoki, W., & Christlieb, N. 2008, in *AIP Conf. Proc. 990: First Stars III*, 167
- Kupka, F., Piskunov, N., Ryabchikova, T. A., Stempels, H. C., & Weiss, W. W. 1999, *A&AS*, 138, 119
- Kurucz, R. L. 1992, *Rev. Mex. Astron. Astrofis.*, 23, 181
- Kurucz, R. L. 1993, *Kurucz CD-ROMs, Vol. 2–12, Opacities for Stellar Atmospheres* (Cambridge, Mass.: SAO)
- Kurucz, R. L. 1993, *Kurucz CD-ROM 15, Diatomic Molecular Data for Opacity Calculations*, Cambridge: SAO
- Mashonkina, L., Korn, A. J., & Przybilla, N. 2007, *A&A*, 461, 261
- Meynet, G., Ekström, S., & Maeder, A. 2006, *A&A*, 447, 623
- Meynet, G. & Maeder, A. 2002, *A&A*, 390, 561
- Mihalas, D., Däppen, W., & Hummer, D. G. 1988, *ApJ*, 331, 815
- Nordlund, Å. 1982, *A&A*, 107, 1
- Norris, J. E., Christlieb, N., Korn, A. J., Eriksson, K., Bessell, M. S., Beers, T. C., Wisotzki, L., & Reimers, D. 2007, *ApJ*, 670, 774
- Piau, L., Beers, T. C., Balsara, D. S., Sivarani, T., Truran, J. W., & Ferguson, J. W. 2006, *ApJ*, 653, 300
- Piskunov, N. E. & Valenti, J. A. 2002, *A&A*, 385, 1095
- Ryan, S. G., Norris, J. E., & Beers, T. C. 1999, *ApJ*, 523, 654

Sauval, A. J. & Tatum, J. B. 1984, *ApJS*, 56, 193

Snedden, C., Cowan, J., Burris, D., & Truran, J. 1998, *ApJ*, 496, 235

Spiegel, D. N., Bean, R., Doré, O., Nolta, M. R., Bennett, C. L., Dunkley, J., Hinshaw, G., Jarosik, N., Komatsu, E., Page, L., Peiris, H. V., Verde, L., Halpern, M., Hill, R. S., Kogut, A., Limon, M., Meyer, S. S., Odegard, N., Tucker, G. S., Weiland, J. L., Wollack, E., & Wright, E. L. 2007, *ApJS*, 170, 377

Stein, R. F., & Nordlund, Å. 1998, *ApJ*, 499, 914

Tominaga, N., Maeda, K., Umeda, H., Nomoto, K., Tanaka, M., Iwamoto, N., Suzuki, T., & Mazzali, P. A. 2007, *ApJ*, 657, L77

Umeda, H. & Nomoto, K. 2003, *Nature*, 422, 871

Table 1. Measured S/N ratios in different wavelength regions

λ (\AA)	S/N (pixel)	Setting	Pixel size (km s^{-1})	FWHM of Th-Ar lines (pixel)
~ 3500	~ 170	BLUE 346 nm	~ 2.7	~ 3.8
~ 3800	~ 250	BLUE 346 nm	~ 2.4	~ 3.7
~ 5000	~ 470	RED 580 nm	~ 2.3	~ 3.2
~ 6000	~ 750	RED 580 nm	~ 2.4	~ 3.5
~ 6700	~ 600	RED 580 nm	~ 2.1	~ 3.5
~ 8500	~ 200	RED 760 nm	~ 2.3	~ 3.4

Table 2. VLT/UVES abundances of HE 1327–2326

Species	$\log \epsilon(X)_{\odot}$	$N_{\text{lin.}}^{\text{a}}$	$\log \epsilon(X)_{1\text{D}}$	$\log \epsilon(X)_{3\text{D}}$	$[X/H]_{3\text{D}}$	$[X/Fe]_{3\text{D}}$
C (CH)	8.39	syn	6.90	6.21	–2.18	3.78
N (NH)	7.78	syn	6.79	6.10	–1.68	4.28
O (OH)	8.66	syn	6.84	6.12	–2.54	3.42
Na I	6.17	2	2.99	2.94	–3.23	2.73
Mg I	7.53	4	3.54	3.54	–3.99	1.97
Al I	6.37	1	1.90	1.87	–4.50	1.46
Ca I	6.31	1	0.88	0.79	–5.52	0.44
Ca II	6.31	4	1.34	1.26	–5.05	0.91
Ti II	4.90	15	–0.09	–0.15	–5.05	0.91
Fe I	7.45	12	1.79	1.49	–5.96	...
Ni I	6.23	4	0.73	0.45	–5.78	0.18
Sr II	2.92	2	–1.76	–1.87	–4.79	1.17
Li I	1.05	6707	< 0.70	< 0.62
Be II	1.38	3131	< –1.20	< –1.15
Sc II	3.05	3613	< –1.68	< –1.80	< –4.85	< 1.11
V I	4.00	3184	< 1.50	< 1.36	< –2.64	< 3.32
Cr I	5.64	3579	< 0.45	< 0.26	< –5.38	< 0.58
Mn I	5.39	3439	< 0.84	< 0.55	< –4.84	< 1.12
Fe II	7.45	3227	< 1.99	< 2.05	< –5.40	< 0.56
Co I	4.92	3454	< 0.58	< 0.31	< –4.61	< 1.35
Zn I	4.60	4810	< 1.61	< 1.65	< –2.95	< 3.01
Ba II	2.17	4554	< –2.14	< –2.39	< –4.56	< 1.40
Eu II	0.52	6645	< –0.76	< –0.80	< –1.32	< 4.64

Note. — All $[X/Fe]$ 3D ratios are computed with $[Fe/H] = -5.96$. Solar abundances have been taken from Asplund et al. (2005).

^a“Syn” indicates the use of spectrum synthesis for the abundance determination. For upper limits the wavelength of the employed line is given.

^b3D CNO corrections have been determined from spectrum synthesis, see text for details.

Table 3. Atomic data and measured equivalent widths

Species	λ (Å)	χ (eV)	$\log gf$ (dex)	W_λ		$\log \epsilon(1D)$	$\log \epsilon(3D)$
				This work (mÅ)	Aoki et al. (mÅ)		
Na I	5889.951	0.00	0.12	53.8	48.9	2.99	2.93
Na I	5895.924	0.00	-0.18	33.6	31.5	2.99	2.94
Mg I	3829.355	2.71	-0.21	23.9	22.6	3.48	3.50
Mg I	5167.321 ^a	2.71	-1.03	8.4	9.8	3.68	3.68
Mg I	5172.684	2.71	-0.40	20.9	21.1	3.50	3.49
Mg I	5183.604	2.72	-0.18	30.4	30.1	3.50	3.49
Al I	3961.529	0.01	-0.34	b	11.0	1.92	1.87
Ca I	4226.728	0.00	0.24	b	2.7	0.89	0.79
Ca II	3933.663	0.00	0.11	b	128.9	1.31	1.16
Ca II	8498.023	1.69	-1.42	10.0	...	1.31	1.28
Ca II	8542.091	1.70	-0.46	54.7	...	1.38	1.29
Ca II	8662.141	1.69	-0.72	39.1	...	1.36	1.31
Ti II	3072.984	0.00	-0.36	5.4	...	0.20	0.11
Ti II	3088.037	0.05	0.25	7.2	...	-0.24	-0.32
Ti II	3229.198	0.00	-0.55	3.5	...	0.17	0.08
Ti II	3234.520	0.05	0.43	10.1	7.2	-0.27	-0.34
Ti II	3236.578	0.03	0.23	6.8	...	-0.29	-0.38
Ti II	3239.044	0.01	0.06	7.5	...	-0.08	-0.17
Ti II	3241.994	0.00	-0.05	3.9	...	-0.30	-0.39
Ti II	3322.941	0.15	-0.09	3.8	...	-0.13	-0.22
Ti II	3349.408	0.05	0.59	15.3	16.6	-0.23	-0.33
Ti II	3372.800	0.01	0.27	13.5	...	-0.02	-0.12
Ti II	3380.279	0.05	-0.57	4.8	...	0.36	0.27
Ti II	3383.768	0.00	0.14	9.1	...	-0.10	-0.20
Ti II	3387.846	0.03	-0.43	5.1	...	0.23	0.13
Ti II	3759.296	0.61	0.27	4.9	5.9	-0.04	-0.08
Ti II	3761.323	0.57	0.17	2.7	4.7	-0.24	-0.28
Fe I	3440.606	0.00	-0.67	5.1	...	1.86	1.48
Fe I	3440.989	0.05	-0.96	3.0	...	1.80	1.43
Fe I	3581.193	0.86	0.42	6.2	5.9	1.75	1.56

Table 3—Continued

Species	λ (Å)	χ (eV)	$\log gf$ (dex)	W_λ		$\log \epsilon(1D)$	$\log \epsilon(3D)$
				This work (mÅ)	Aoki et al. (mÅ)		
Fe I	3618.768	0.99	0.00	1.2:	...	1.53: ^c	1.36
Fe I	3719.935	0.00	-0.43	7.9	...	1.85	1.48
Fe I	3737.131	0.05	-0.57	4.5	3.9	1.76	1.41
Fe I	3745.561	0.09	-0.77	3.9	4.8	1.82	1.48
Fe I	3748.262	0.11	-1.02	1.9	...	1.86	1.53
Fe I	3758.233	0.96	-0.01	2.0	5.1	1.69	1.54
Fe I	3820.425	0.86	0.16	3.4	2.5	1.66	1.49
Fe I	3825.881	0.92	-0.04	1.8:	...	1.58: ^c	1.43
Fe I	3856.372	0.05	-1.29	1.1:	...	1.79: ^c	1.43
Fe I	3859.912	0.00	-0.71	4.8	6.8	1.83	1.45
Fe I	4045.812	1.49	0.29	b	1.9	1.78	1.68
Ni I	3414.761	0.03	-0.03	2.9	< 7.5	0.70	0.40
Ni I	3515.049	0.11	-0.21	2.1	...	0.81	0.53
Ni I	3524.535	0.03	0.01	2.4	...	0.57	0.26
Ni I	3619.386	0.42	0.04	2.0	...	0.83	0.61
Sr II	4077.724	0.00	0.16	b	7.3	-1.76	-1.87
Sr II	4215.540	0.00	-0.16	b	3.8	-1.75	-1.86
Li I	6707.761	0.00	-0.01	syn ^d	...	< 0.70	0.62
Li I	6707.912	0.00	-0.31	syn ^d	...	< 0.70	0.62
Be II	3130.420	0.00	-0.17	syn ^d	...	< -1.20	-1.15
Be II	3131.065	0.00	-0.47	syn ^d	...	< -1.20	-1.15
[O I]	6300.304	0.00	-9.82	< 1.8	...	< 8.01	< 8.07
O I	7771.944	9.15	0.32	< 2.0	...	< 6.19	< 6.21
O I	7774.166	9.15	0.17	< 2.0	...	< 6.34	< 6.36
O I	7775.388	9.15	-0.05	< 2.0	...	< 6.56	< 6.58
Sc II	3572.526	0.02	0.27	< 1.1	...	< -1.57	< -1.68
Sc II	3613.829	0.02	0.42	< 1.0	...	< -1.68	< -1.80
Sc II	3642.784	0.00	0.13	< 1.2	...	< -1.45	< -1.54
VI	3183.410	0.02	0.46	< 2.6	...	< 1.60	< 1.46
VI	3183.970	0.04	0.58	< 2.6	...	< 1.50	< 1.36

Table 3—Continued

Species	λ (Å)	χ (eV)	$\log gf$ (dex)	W_λ		$\log \epsilon(1D)$	$\log \epsilon(3D)$
				This work (mÅ)	Aoki et al. (mÅ)		
VI	3184.013	0.00	0.34	< 2.6	...	< 1.70	< 1.54
Cr I	3578.684	0.00	0.41	< 1.2	...	< 0.45	< 0.26
Cr I	3593.481	0.00	0.31	< 1.3	...	< 0.59	< 0.40
Cr I	4254.332	0.00	−0.11	b	< 2.0	< 1.07	< 0.88
Mn I	4030.753	0.00	−0.47	b	< 2.0	< 0.84	< 0.55
Fe II	3227.742	1.67	−1.10	< 2.2	...	< 1.99	< 2.05
Fe II	5018.450	2.89	−1.22	< 0.8	< 2.0	< 2.61	< 2.66
Co I	3453.514	0.43	0.38	< 1.5	< 6.3	< 0.58	< 0.31
Zn I	4810.528	4.08	−0.15	< 1.0	< 2.0	< 1.61	< 1.65
Ba II	4554.029	0.00	0.17	b	< 1.8	< −2.14	< −2.39
Ba II	4934.100	0.00	−0.16	< 1.1	...	< −2.04	< −2.23
Eu II	6645.064	1.38	0.21	< 1.1	...	< −0.76	< −0.80

^aThe blend with an Fe line is negligible.

^bThese lines are not covered by the new VLT data.

^cThese lines are not included in the final abundance estimate.

^dAbundance limit was derived from spectrum synthesis.

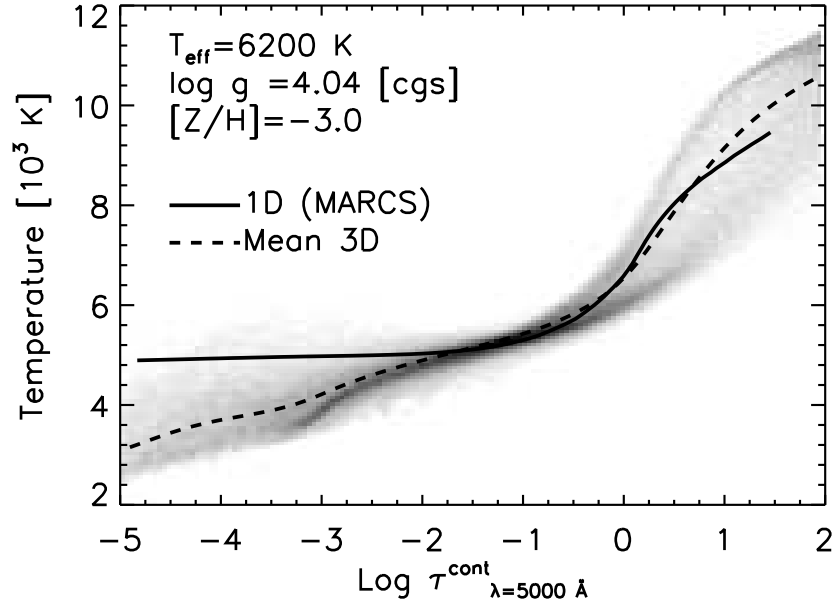


Fig. 1.— Temperature structure the upper layers of the 3D hydrodynamical simulation adopted in the present 3D–1D differential abundance analysis. *Gray shaded area*: temperature distribution as a function of optical depth at 5000 \AA in the 3D model. Darker areas indicate temperature values with higher probability. *Dashed line*: mean temperature stratification of the simulation (averaged over surfaces of constant optical depth at 5000 \AA). *Solid line*: temperature stratification of the 1D MARCS model constructed for the same stellar parameters.

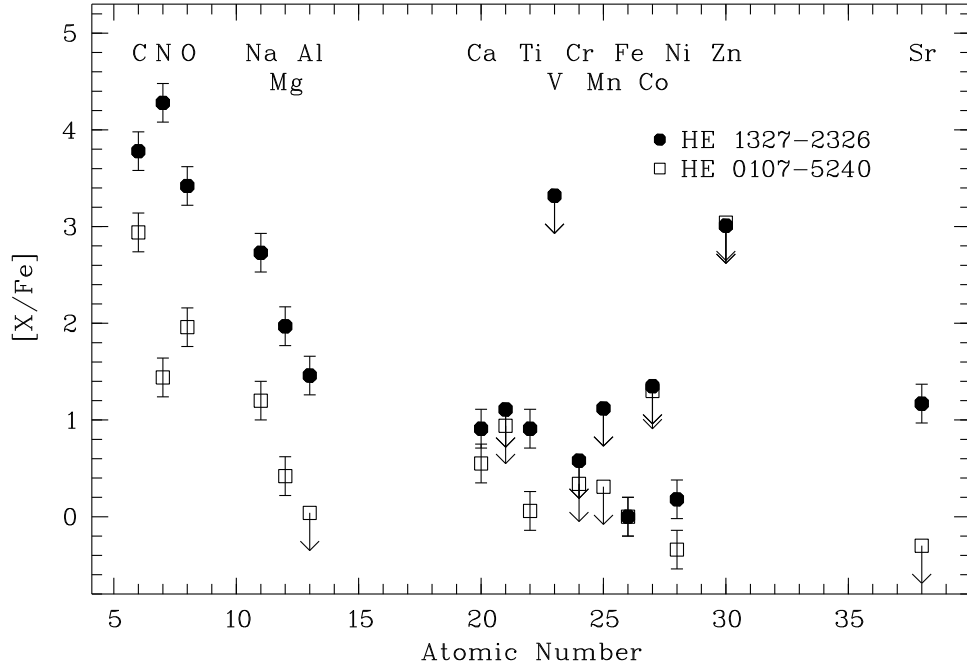


Fig. 2.— Abundance pattern of HE 1327–2326 (*filled circles*) in comparison with that of HE 0107–5240 (*open squares*). Typical 1σ errors of 0.2dex are shown. Upper limits are indicated by an arrow. The 3D abundances for HE 0107–5240 are taken from Collet et al. (2006).

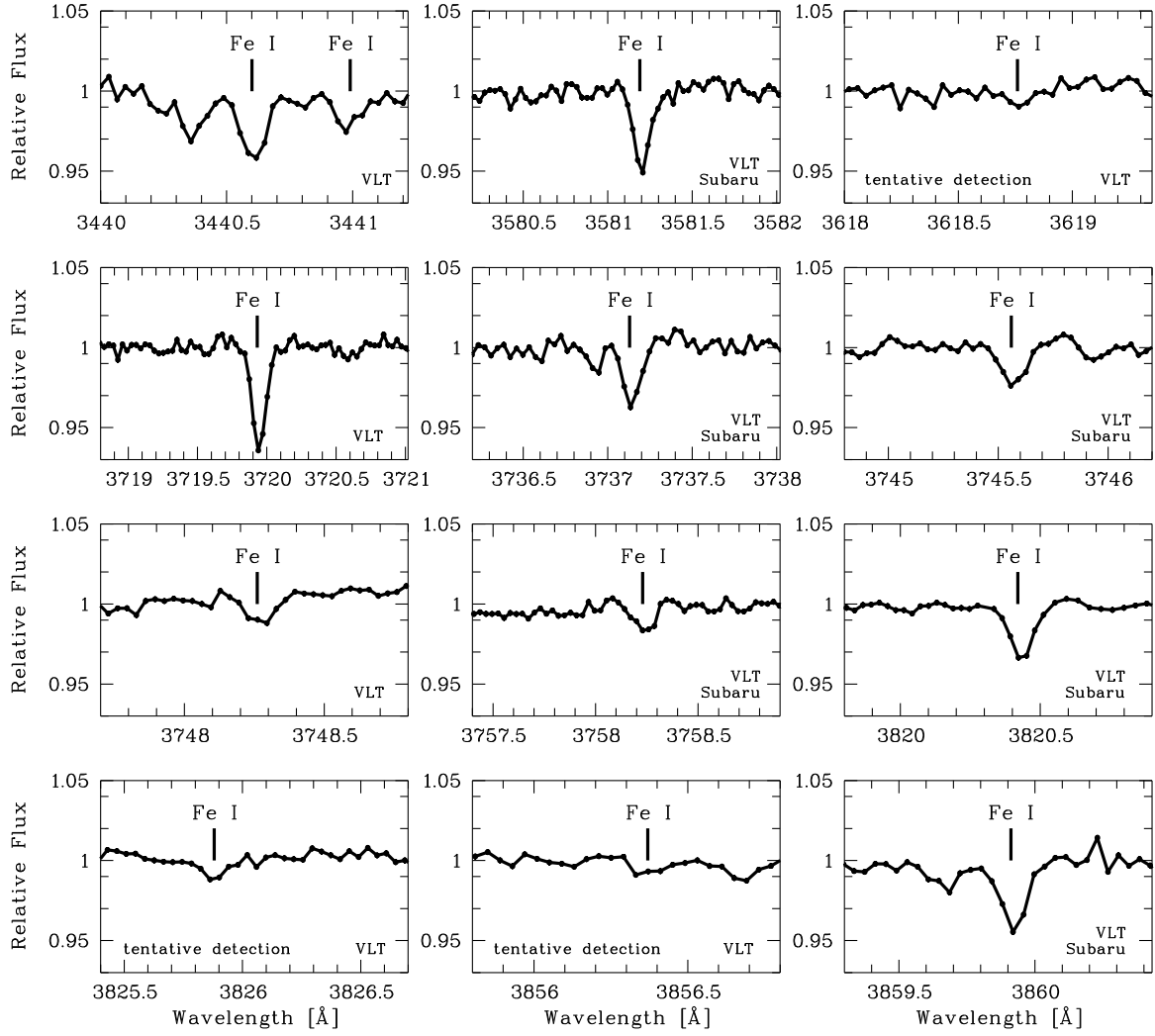


Fig. 3.— All detected and tentatively detected FeI lines in the VLT/UVES spectrum of HE 1327–2326. Equivalent width measurements can be found in Table 3.

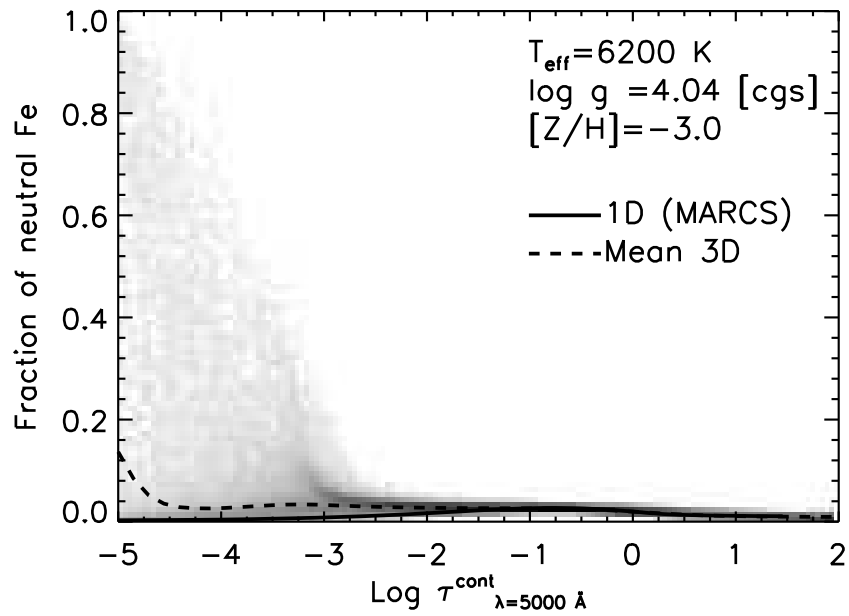


Fig. 4.— Ratio of neutral to total iron number densities ($n_{\text{FeI}}/n_{\text{Fe}}$) as a function of optical depth at 5000 \AA . *Gray shaded area*: distribution of $n_{\text{FeI}}/n_{\text{Fe}}$ values in the 3D model atmosphere adopted here; darker areas indicate values with higher probability. Over-plotted are the curves for the mean 3D stratification (*dashed line*) and for the corresponding 1D MARCS model atmosphere (*solid line*).

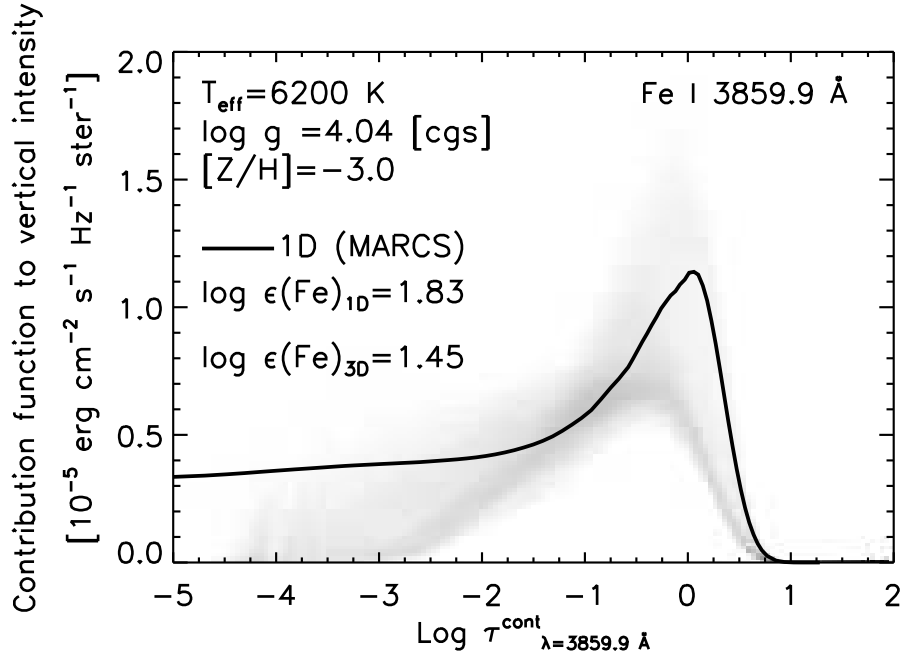


Fig. 5.— Contribution function to outgoing intensity in the vertical direction at line centre for the FeI 3859.9 Å line as a function of optical depth. *Gray shaded area*: distribution of the contribution function values in the 3D model atmosphere adopted here; darker areas indicate values with higher probability. Over-plotted (*solid line*) is the contribution function computed with the corresponding 1D MARCS model. The reported 3D and 1D Fe abundances are the ones reproducing the measured equivalent width of the line.

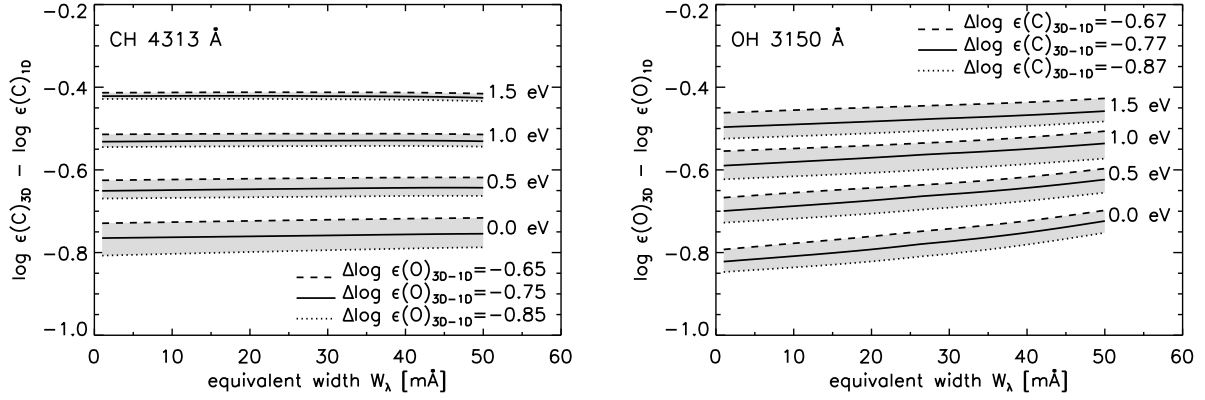


Fig. 6.— 3D–1D LTE corrections to the C (*left panel*) and O abundances (*right panel*) as derived from fictitious CH and OH lines. Carbon and oxygen abundance corrections are plotted as a function of line strength for selected values of the lower excitation potential (0 to 1.5 eV) and for different values of 3D O and C abundances respectively.

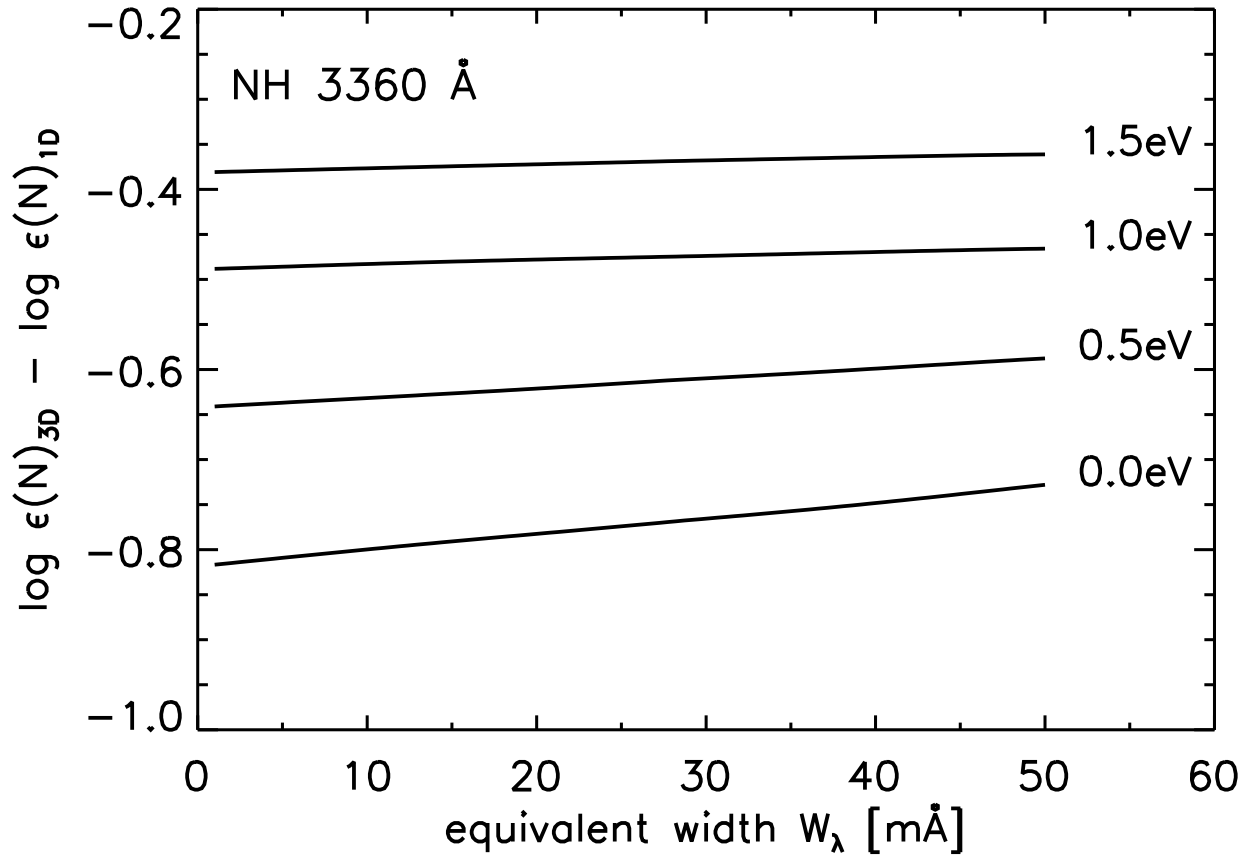


Fig. 7.— 3D–1D LTE corrections to the N abundance as derived from fictitious NH lines. The corrections are plotted as a function of line strength for different values of the lower excitation potential.

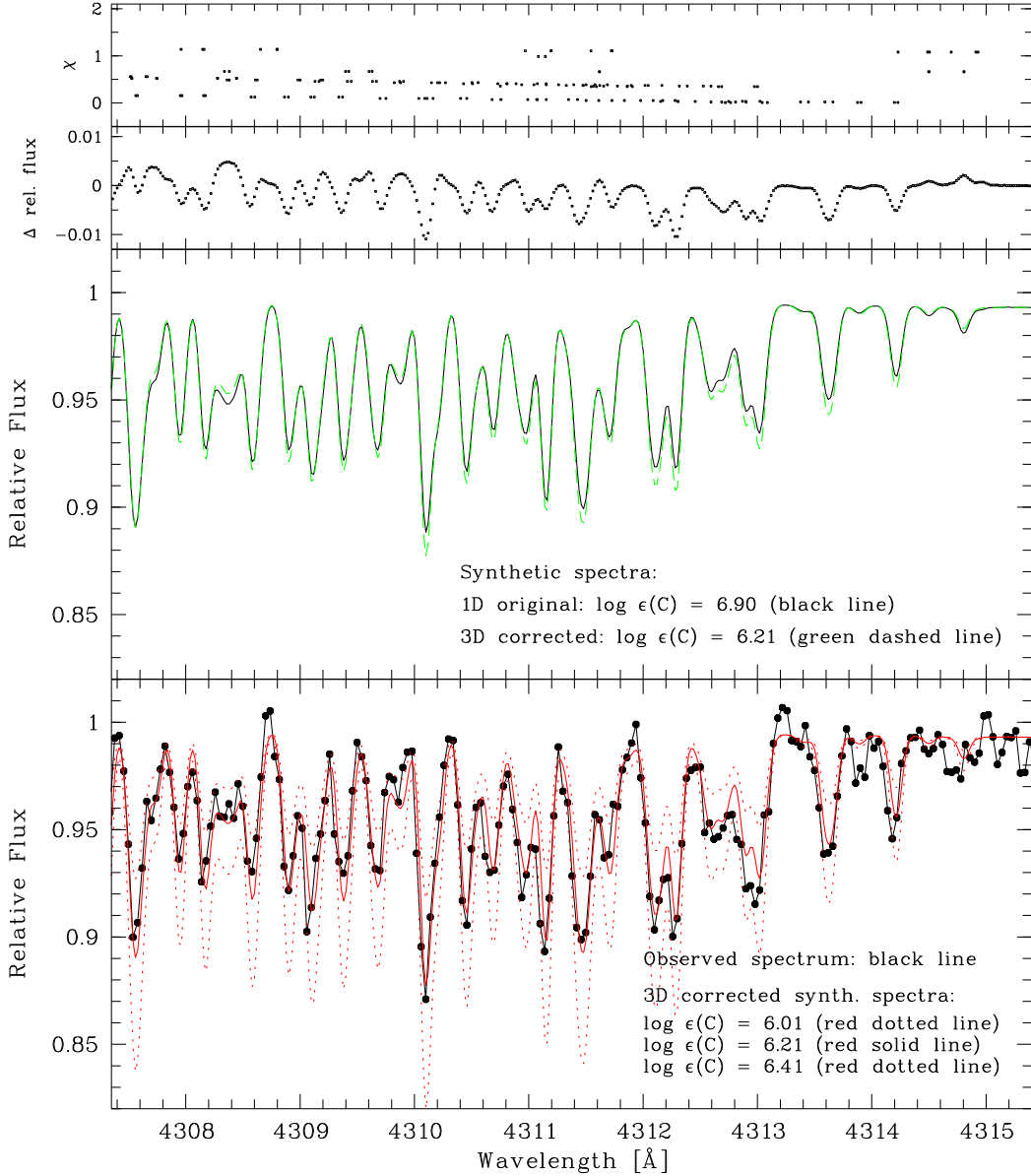


Fig. 8.— CH G-band spectral region of HE 1327–2326. In the top panel, the excitation potentials of the molecular CH lines are presented. In the second panel from the top, the flux difference between the “1D” and “3D-aided” synthetic spectra (from the panel below) is given. A comparison of the “1D” synthetic spectrum with a synthetic spectrum generated from the 3D-adjusted linelist is shown in the second panel from the bottom. The abundance of the “3D-aided” synthetic spectrum was varied to reproduce the “1D” spectrum, and so that the average difference of the two fluxes seen in the panel above becomes zero over the given wavelength range. Abundances are as given. In the bottom panel we show the observed Subaru/HDS spectrum (*dots*) overplotted with “3D-aided” synthetic spectra with C abundances of $[C/Fe] = 3.78$ (*solid line*), 3.58, and 3.98 (*dotted lines*). The average 3D–1D correction over this wavelength range for CH is -0.69 dex.

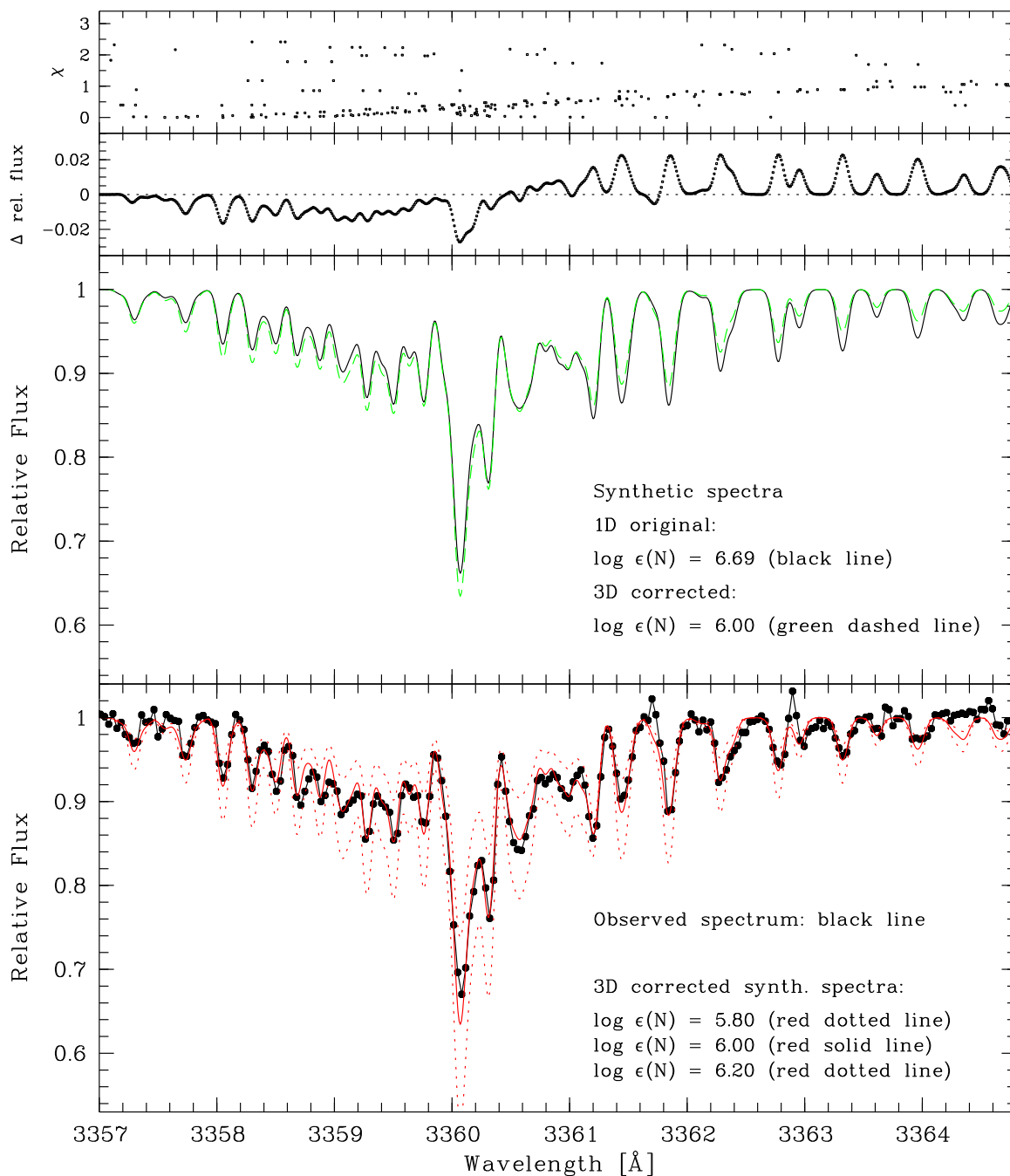


Fig. 9.— Same as for Figure 8, but for the NH spectral region. The observed VLT/UVES spectrum (*dots*) in the bottom panel is overplotted with “3D-aided” synthetic spectra with N abundances of $[N/Fe] = 4.28$ (*solid line*), 4.08, and 4.48 (*dotted lines*). The average 3D–1D correction over this wavelength range for NH is -0.69 dex.

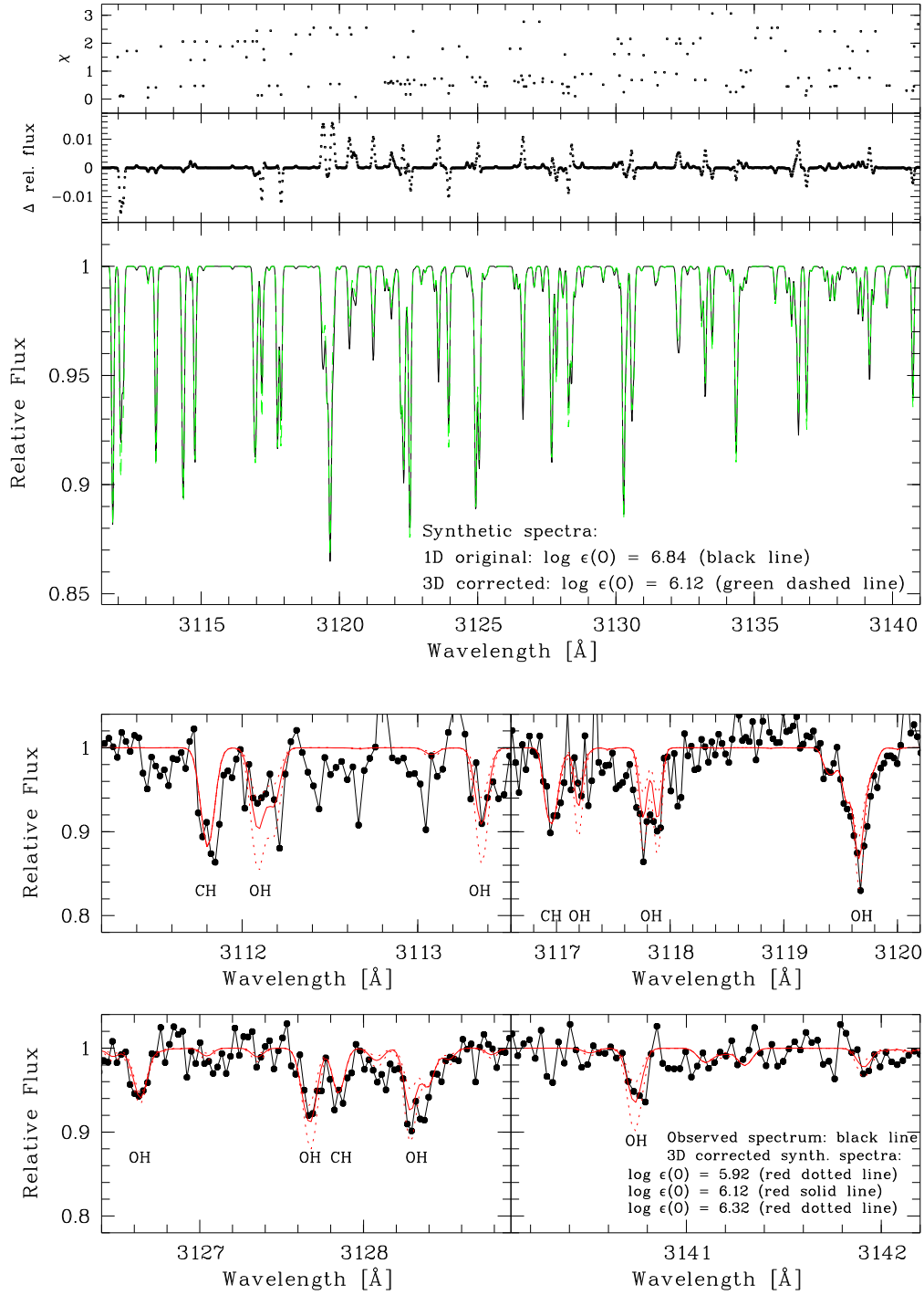


Fig. 10.— Same as for Figure 8, but for several spectral region with OH lines. The observed VLT/UVES spectrum (*dots*) in the two panels at the bottom is overplotted with “3D-aided” synthetic spectra with O abundances of $[O/Fe] = 3.42$ (*solid line*), 3.22, and 3.62 (*dotted lines*). The average 3D–1D correction over this wavelength range for OH is -0.72 dex.

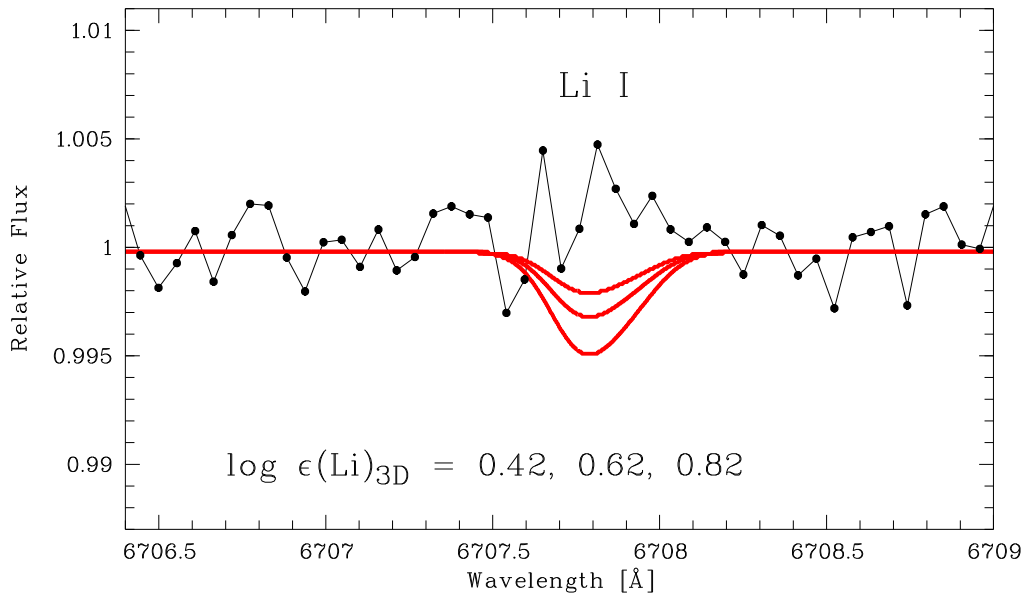


Fig. 11.— Spectral region (*connected dots*) of the Li I doublet at 6707 Å in HE 1327–2326. Synthetic spectra are overplotted (*solid lines*) for three Li abundances. The upper limit is $A(\text{Li}) < 0.62$.

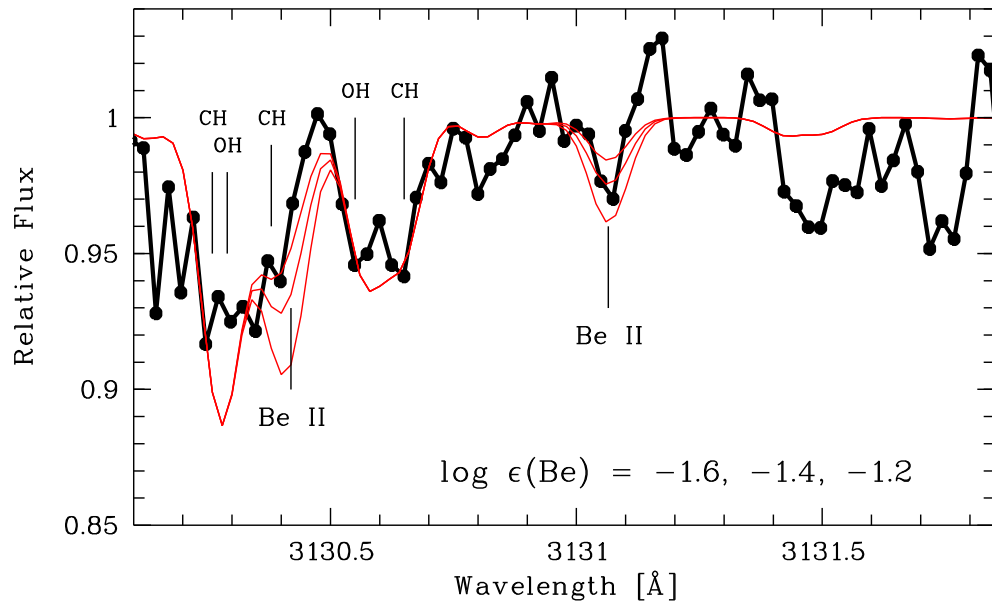


Fig. 12.— Spectral region (*connected dots*) of the two beryllium lines at $\sim 3130 \text{ \AA}$ in HE 1327–2326. Synthetic spectra are overplotted (*solid lines*) for three Be abundances. The upper limit derived from both lines is $\log \epsilon(\text{Be}) < -1.2$.

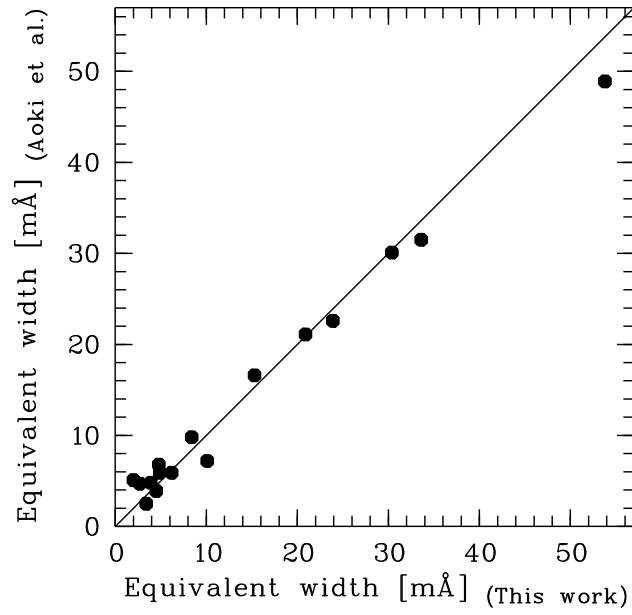


Fig. 13.— Comparison of the equivalent width measurements between this work and Aoki et al. (2006).

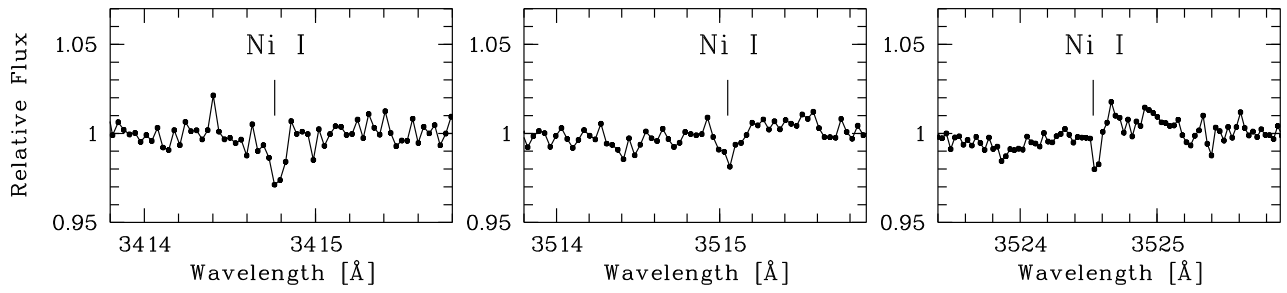


Fig. 14.— Three of the four detected NiI lines in the VLT/UVES spectrum of HE 1327–2326.

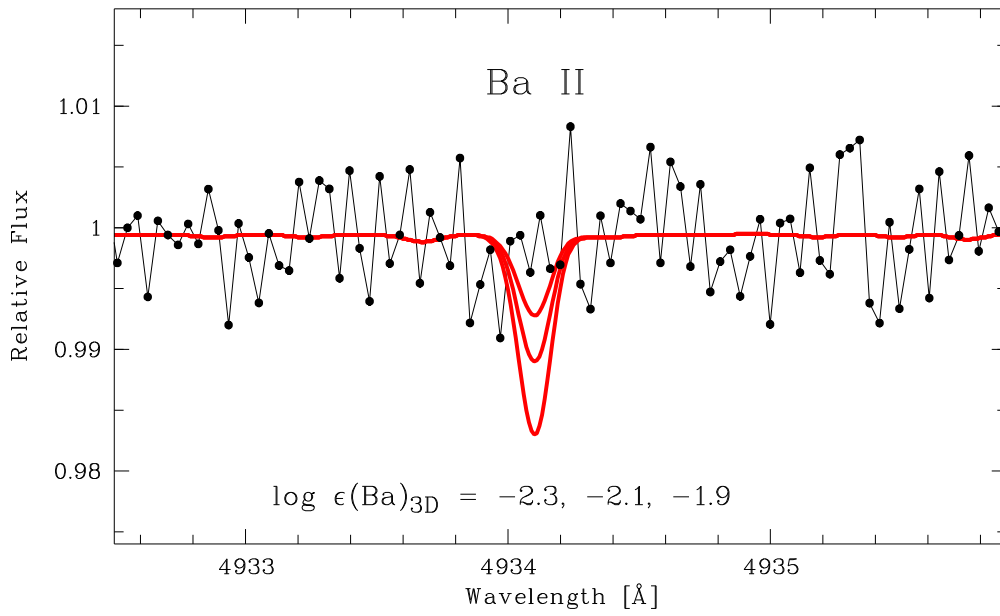


Fig. 15.— Spectral region (*connected dots*) of the barium line at 4937 Å in HE 1327–2326. Synthetic spectra are overplotted (*solid lines*) for three Ba abundances. The upper limit for this line is $\log \epsilon(\text{Ba}) < -2.04$.

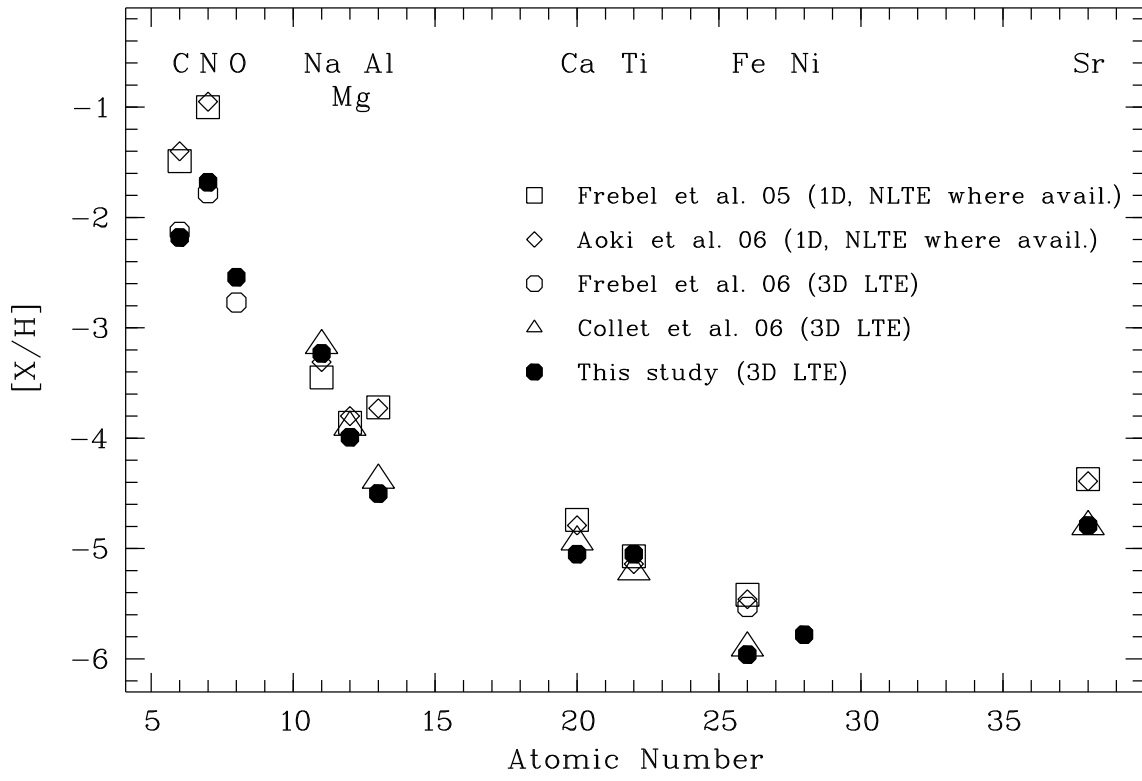


Fig. 16.— Comparison of previously published abundances $[X/H]$ of HE 1327–2326.

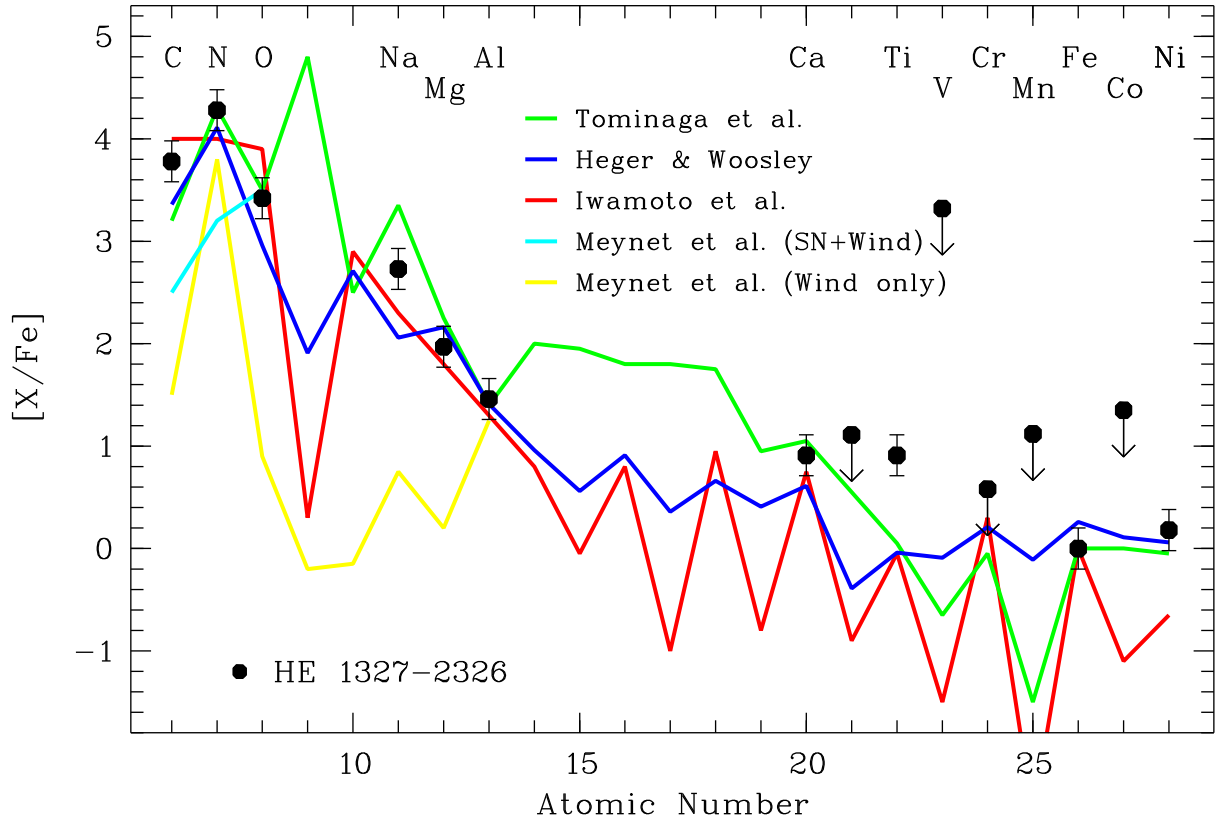


Fig. 17.— Comparison of the new 3D-1D corrected abundances $[X/Fe]$ of HE 1327-2326 with predictions from various models based on chemical yields of the first-generation SNe. See text for discussion.

